UNLV Theses, Dissertations, Professional Papers, and Capstones

8-1-2018

The Effect of Titanium Dioxide on Nucleate Pool Boiling Using an Aluminum Substrate

Kevin Yim
kevin.y.yim@gmail.com

THE EFFECT OF TITANIUM DIOXIDE ON NUCLEATE POOL BOILING USING

AN ALUMINUM SUBSTRATE

By

Kevin Yim

Bachelor of Science in Engineering – Mechanical Engineering
University of Nevada, Las Vegas
2014

A thesis submitted in partial fulfillment
of the requirements for the

Master of Science in Engineering – Mechanical Engineering

Department of Mechanical Engineering
Howard R. Hughes College of Engineering
The Graduate College

University of Nevada, Las Vegas
August 2018

Thesis Approval

The Graduate College
The University of Nevada, Las Vegas

May 31, 2018

This thesis prepared by

Kevin Yim

entitled

The Effect of Titanium Dioxide on Nucleate Pool Boiling Using an Aluminum Substrate

is approved in partial fulfillment of the requirements for the degree of

Master of Science in Engineering – Mechanical Engineering
Department of Mechanical Engineering

Kwang Kim, Ph.D.   Kathryn Hausbeck Korgan, Ph.D.
Examination Committee Chair   *Graduate College Interim Dean*

Brendan O' Toole, Ph.D.
Examination Committee Member

Hui Zhao, Ph.D.
Examination Committee Member

Jacimaria Batista, Ph.D.
Graduate College Faculty Representative

ii

Abstract

Nucleate pool boiling is a mode of pool boiling that tends to transfer heat more efficiently than the other modes of pool boiling. Many studies have been done to augment the heat transferred during nucleate pool boiling. Various methods of heat transfer augmentation in boiling can be performed through active treatments (mechanical aids, surface/fluid vibrations, etc.) or passive treatments (functional coating, surface roughening, etc.). This study focuses primarily on a passive treatment, specifically TiO_2 coating, which involves testing a substrate coated with TiO_2 using NeverWet[TM] base coating as a coupling agent and coated using a method outlined by Wu et al. [7]. The results are evaluated by comparing the overall boiling curve and heat transfer coefficient with other baseline samples for water. Anatase TiO_2 was chosen as the material for this study because it is naturally hydrophilic, and interestingly, it can become super-hydrophilic after being exposed to ultraviolet light at a wavelength of less than 380 nm. The focus, however, is on its physical properties.

A large factor for heat transfer in nucleate pool boiling is the formation of bubbles, bubble release, and the number of active nucleation sites on the sample. Nucleation sites can only be active for a favorable geometry (the cavity radius must be within a specific range) and must be within an area of influence where the waiting period of the site is less than the rest of the cavities. The water contact angle of the sample and the tilt angle of the sample also influences the formation and detachment of the bubbles on the sample. Based on this information, this study investigates cylindrical samples coated with TiO_2. With a lower contact angle, the cylindrical sample yielded more active nucleation sites which resulted in enhancement of heat transfer in nucleate pool boiling conditions. The TiO_2 without the coupling agent yielded an 8% improvement in critical heat flux as opposed to the baseline Al 6061 substrate. This enhancement

was backed up using image processing to gather bubble departure frequency and bubble diameter data to use on a current vapor-exchange model – this model and the experimental data was compared in this study. The bubble departure frequency was significantly higher in TiO_2 coated substrate than the baseline sample, while the bubble diameters, overall, were lower, thus agreeing with the analytical models of the roles of interfacial tension in bubble formation and departure.

Acknowledgements

First, I would like to thank my advisor, Dr. Kwang Kim, who has exercised great patience with me and provided me with much support, insight, mentorship, and guidance. I will forever be grateful for the opportunity I have had in his laboratory and the experiences I have had under his supervision.

Next, I'm thankful for my fellow lab members, friends, colleagues, girlfriend, and family for the constant support they have given me through my years here. I would especially like to thank Blake Naccarato for the assistance he has given me by helping me with the video processing and the advice he has given me throughout my work. I would also like to thank those who have helped me with machining my pool boiling chamber and samples, including Tony Filipiak, Andrew Poland, and Zachary Frank.

Also, I would like to thank my committee members, Dr. Hui Zhao, Dr. Brendan O'Toole, and Dr. Jaci Batista for taking the time to serve as my committee members.

Lastly, I would like to acknowledge and dedicate this thesis to my mother, Young Ran Yim. She had always conveyed to me the importance of a strong education and she had always pushed me to strive to be the best academically and intellectually. Her overwhelming support and encouragement is the reason why I pursued a college education and now, graduate studies. I will forever be grateful for her efforts to push me to be the greatest person that I can be.

Table of Contents

List of Figures

Nomenclature

A	area	*Greek Characters*	
B	buoyance	α	angle of a tilted surface
d	diameter	γ	interfacial tension on a bubble
f	force	Δ	uncertainty
f	bubble frequency departure	δ	thermal boundary
G	image gradient	$\pi\phi$	circular contact base of a bubble
G_x	image gradient x-direction	ρ	density
G_y	image gradient y-direction	θ	contact angle
h	heat transfer coefficient	$\theta_{saturation}$	bubble saturation temperature
h_{lv}	latent heat of vaporization	$\theta_{surface}$	bubble surface temperature
I	current	σ	surface tension
k	thermal conductivity		
L	length		
N_a	active nucleation sites		
p	pressure		
Q	heat		
Q_{loss}	heat loss		
$q"$	heat flux		
R	thermal resistance		
r	radius		
r_c	cavitiy radius		
r_n	bubble radius		
s	entropy		
T	temperature		
$T_{ambient}$	ambient temperature		
$T_{saturation}$	saturation temperature		
$T_{surface}$	surface temperature		
U	internal energy		
V	voltage		
v	specific volume		

Chapter 1. Introduction

1.1. General overview of pool boiling

Pool boiling occurs when a heated surface is submerged in a body of liquid. Pool boiling has applications in thermal management systems such as refrigeration and boiling, heat dissipation in various systems, and nuclear reactors. Generally, heat transfers more efficiently during nucleate pool boiling, so these applications can benefit from increased pool boiling efficiency by saving on energy input. The pool boiling curve is generated from a correlation of the heat flux applied to the surface and the wall superheat, which is the temperature difference between the surface of the boiling surface and the saturation temperature of the working fluid. The relationship between the heat flux and wall superheat can be seen in Equation (1.1):

$$q'' = h(T_{surface} - T_{saturation}) \tag{1.1}$$

where q'' is heat flux, h is the boiling heat transfer coefficient, $T_{surface}$ is the temperature of the boiling surface, $T_{saturation}$ is the saturation temperature of the working fluid, and the wall superheat is the difference between $T_{surface}$ and $T_{saturation}$ [1].
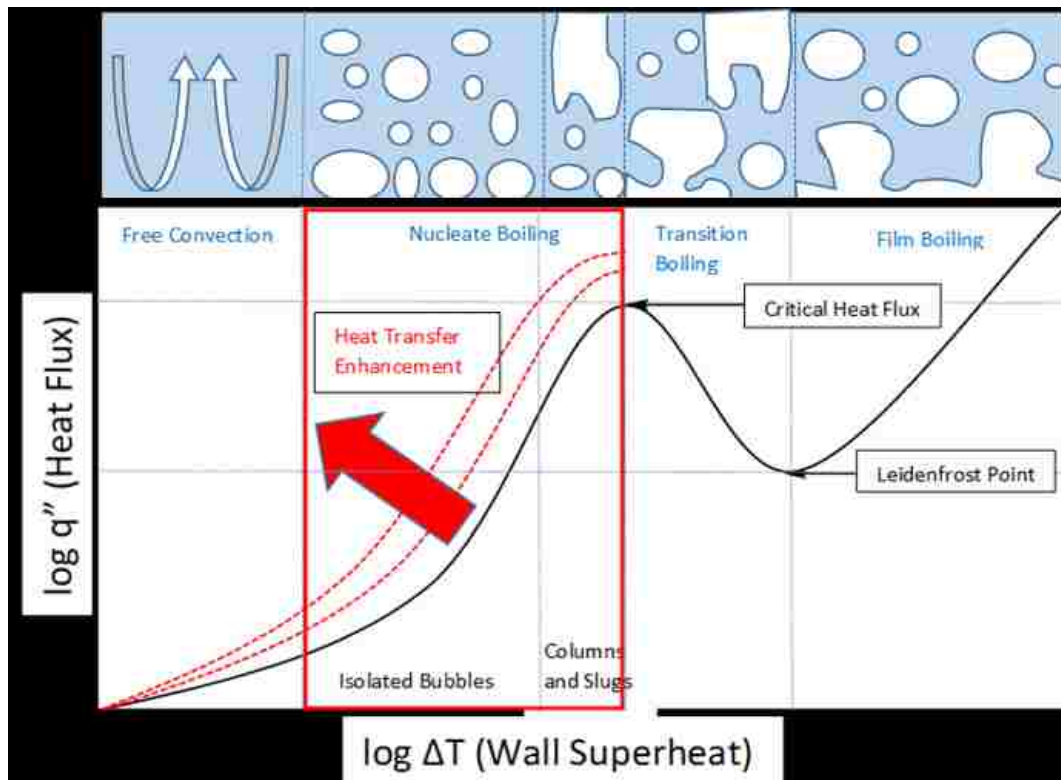
Figure 1.1: General pool boiling curve with graphics of bubble formation in each phase.

There are four different modes to pool boiling based on the trends of the boiling curve: free convection boiling, nucleate pool boiling, transition boiling, and film boiling. Free convection boiling starts to occur when the surface temperature is slightly over the saturation temperature; bubbles begin to form during this stage. As the surface temperature increases even further, nucleate boiling begins to occur. The nucleate boiling onset can be visually observed as bubbles start to emerge from nucleation points of the surface. As the wall superheat starts to increase, more nucleation sites become active, eventually leading to the emergence of many bubbles around the heated surface – this phase of nucleate boiling is categorized as columns and slugs. During nucleate boiling, as the wall superheat increases, the heat flux eventually reaches its highest peak – this is known as the Critical Heat Flux (CHF). Once the working fluid passes the CHF, transition boiling begins to occur – this can be observed because bubbles are forming

rapidly and beginning to form vapor films on the surface. After further increasing the wall superheat, eventually, the fluid will reach the Leidenfrost point, where the heat flux is at a minimum and the boiling surface is covered by a vapor blanket – once the fluid has passed this point, film boiling occurs and heat is transferred through conduction and radiation of the vapor film [1].

When the heat flux increases beyond the critical heat flux, heat transfer is severely limited. This is called boiling crisis. When the heat flux approaches the CHF, dry spots on the heated surface form continuously and are rewetted by the surrounding working liquid. Boiling crisis is characterized when one or more of these localized dry spots spread irreversibly. Figure 1.2 displays an illustration of bubble formation and rewetting of a dry spot during nucleate pool boiling.
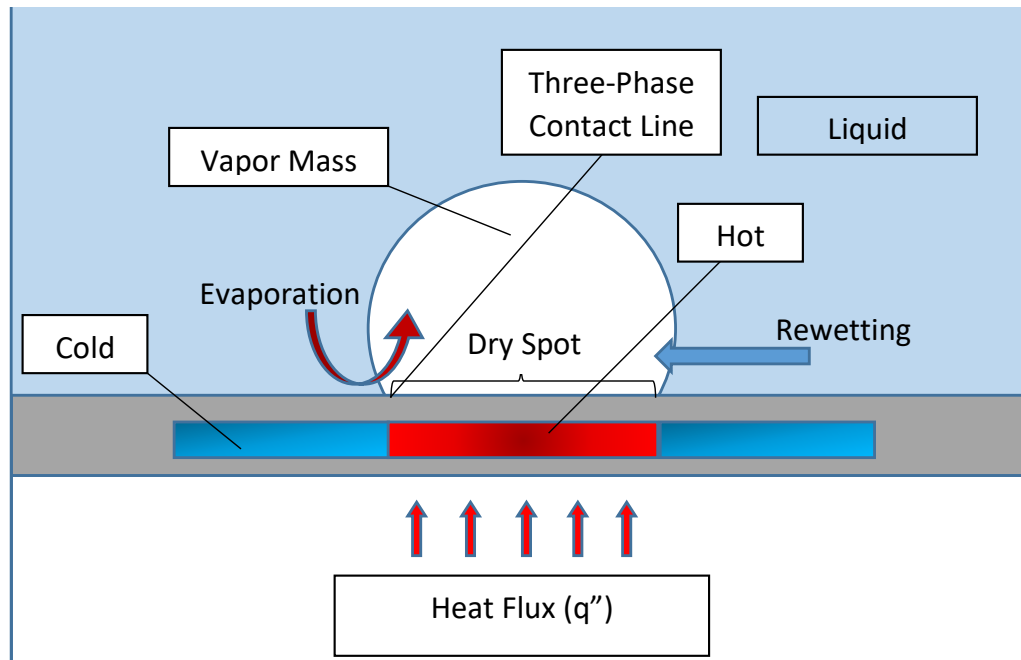
Figure 1.2: Illustration of a dry spot formation in nucleate pool boiling.

Boiling crisis can be delayed through the implementation of active techniques, such as vibrations or electrostatic fields, or through passive techniques such as surface roughening and other surface treatments.

Forster and Greif [2] broke down boiling heat transfer into four mechanisms: micro-convection in the sublayer, the bubbles behavior, latent heat transport by bubbles, and vapor-liquid exchange. The first mechanism is the micro-convection in the sublayer; Forster and Greif discuss that thermal conduction cannot adequately account for large heat fluxes and that the liquid velocity that is induced by bubble growth is large enough to determine temperature distribution in the sublayer near the heat source. They also mention that the wall superheat is the driving potential for heat flux, as shown in Equation (1.1). For mechanism 2, Forster references Sabersky and Mulligan [3] who performed experiments based on a suggestion by H.S. Tsien [4] that bubbles act as surface roughness during boiling heat transfer with forced convection; therefore, increasing turbulent exchange of liquid between the surface and liquid. In mechanism

3, Forster discusses the transport of latent heat of vaporization through bubbles. Lastly, in mechanism 4, Forster discusses that the bubbles also transfer heat during their growth by pushing hot liquid from the heating surface into the stream. Out of the four mechanisms, however, it appears that Forster believed that the first mechanism was the largest contribution to boiling heat transfer, whereas the other three mechanisms have minor contribution towards overall boiling heat transfer.

1.2. Pool boiling heat transfer enhancement through passive treatment techniques

Active techniques for pool boiling heat transfer enhancement generally require mechanical aids; however, this study does not aim to utilize any active techniques. Passive techniques for heat transfer enhancement include use of surface treatments and coatings, adjusting geometries, and utilizing material properties. Previous studies that have been done include experiments done with Dhillon et al. [5] on surface texturing using parametrically designed plain and nano-textured micropillar surfaces, fabrication and testing of aluminum oxide nano-porous surfaces (NPS) conducted by Lee et al. [6], investigation of pool boiling of water and FC-72 on silicon oxide and titanium oxide surface done by Wu et al. [7], and experimentation of various assembled carbon nanotubes and nano-porous structures conducted by Zhang and his coworkers [8–10]. Active techniques may be relevant for future work studies, and will be discussed in the conclusion. Passive techniques are employed in this study such as surface roughening and coating, and factors such as heater geometry and wettability are considered.

1.3. Previous studies with titanium dioxide coating

A study of evaporation and pool boiling using Titanium Dioxide (TiO_2) was first conducted by Takata et al. [11] because of its ability to be both hydrophilic and oleophilic [12]. This means that TiO_2 has an affinity for absorbing water and repelling oils. TiO_2 has two typical crystal structures – anatase and rutile; the anatase structure was the focus of study for Takata. TiO_2 becomes superhydrophilic and gains self-cleaning properties (because the TiO_2 becomes oleophobic and rejects oils) when irradiated by ultraviolet light with a wavelength shorter than 380 nm. This study reported the contact angle of irradiated TiO_2 surfaces to be nearly 0˚ when using the RF Magnetron sputtering process and being irradiated by UV light for 20 hours. Further studies were conducted by Wu et al. [7] focusing on the nucleate pool boiling heat transfer enhancement on titanium oxide and silicon oxide surface. Copper was used as the substrate for the coating. This study reported water contact angles as low as 9˚ for a TiO_2 coated copper surface and CHF enhancement of 50.4% in water and 38.2 in FC-72 and confirmed that the hydrophilicity of the TiO_2 coated surface provided additional enhancement of heat transfer in pool boiling.

1.4. Objectives of the study

The objective of this study is to observe the effects that anatase TiO_2 has on heat transfer during nucleate pool boiling when applied to a horizontal, cylindrical Al 6061 geometry and compare the critical heat flux data of each. Furthermore, this study aims to observe the impact the sample's surface profile has on nucleate pool boiling based on contact angle, cavities, and active nucleation sites through qualitative analysis and the use of video processing through

MATLAB. Lastly, this study aims to verify Forster and Greif's model that compares bubble departure and size with overall heat flux.

1.5. The structure of this thesis

In Chapter 2, the experimental setup is discussed. The chapter entails the design of the pool boiling chamber, the experimental procedures of cleaning the samples and acquiring the necessary data, data reduction, uncertainty analysis, methods of preparing the samples, and contact angle and surface profile information.

Chapter 3 discusses the data acquired experimentally, and visualization information from conducting pool boiling on the various samples. The pool boiling curve for the baseline samples and coated samples are generated and discussed. Furthermore, the visualization method and information is provided for a qualitative view of the differences between the baseline and treated samples.

Finally, Chapter 4 is the conclusion of this thesis. This chapter includes the conclusion that was drawn from experimentation and analysis, more optimal pool boiling chamber designs, and suggested future work. The appendices include supplemental data from the study.

Chapter 2. Experimental Setup

2.1. Pool boiling chamber design and setup

The pool boiling experimentation was completed using the chamber seen in Figure 2.1. The housing consists of stainless steel housing with PTFE plates on each side. The stainless-steel housing was 101.6 mm x 101.6 mm x 177.8 mm and the PTFE plates on each side were 152.4 mm x 152.4 mm with a thickness of 12.7 mm. Insulation was used around the chamber to minimize heat loss within the system. The cylindrical aluminum 6061 samples (diameter of 19.1 mm and length 101.6 mm) length were machined to fit a 400W McMaster-Carr high-temperature cartridge heater in the center of the samples, and T-type thermocouples in the four edges of the surface. This design was based on the pool boiling setup used in Zhang's dissertation [8].
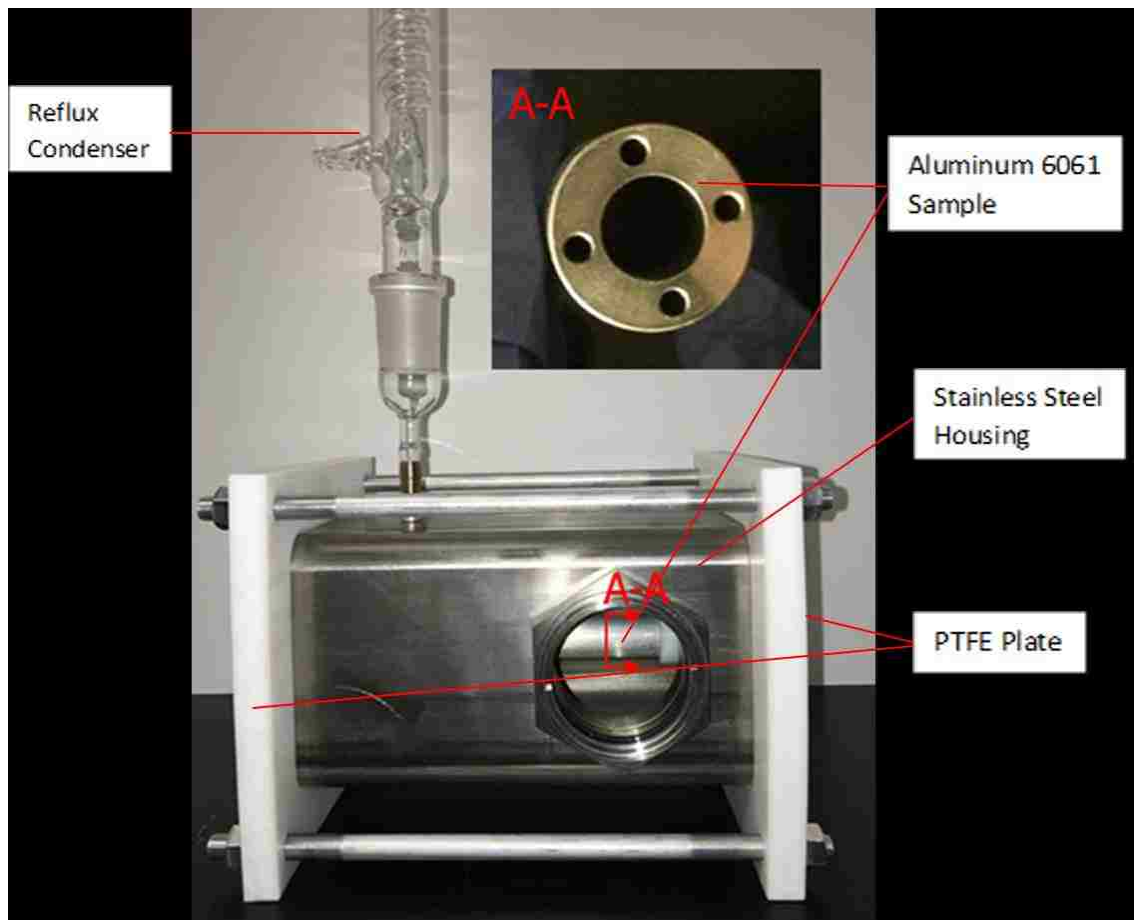
Figure 2.1: Pool boiling chamber experimental setup and Al 6061 heater

Figure 2.2: CAD of the boiling chamber housing and PTFE plates

Aluminum 6061 was used as the base material of the heater samples. Al 6061 is composed of 95.1-98.2% aluminum, and small percentages of chromium, copper, iron, magnesium, manganese, nickel, silicon, titanium, zinc, and zirconium. It has a thermal conductivity of 167 W/m-K, melts at 582°C, and a specific heat capacity of 0.896 J/g- °C. Some common uses of this alloy include: vehicle parts, pipe fittings, and containers [13].

An IO Tech Personal DAQ 56 was used for data acquisition and an Agilent Technologies DC power supply was used to power the heater. The chamber also consisted of an auxiliary heater placed below the sample to increase water temperature to boiling, a T-type thermocouple to monitor the water temperatures, and a reflux condenser was used with a Polyscience constant temperature controller to maintain the volume of water.

2.2. Experimental procedures

The pool boiling chamber and samples were cleaned with acetone and rinsed with DI water prior to conducting the experiment. Afterwards, the thermocouples were calibrated and connected to a HP laptop for data recording. The boiling chamber was assembled, and Omega thermal paste was applied to the cartridge heater and T-type thermocouples and inserted into the sample. Next, the chamber was filled with distilled water and the Polyscience temperature controller was connected to the reflux condenser and turned on. Power was applied at 5 V every 5 minutes to the auxiliary heater to increase the water temperature to saturation, and once the saturation temperature was reached, the power for the cartridge heater was turned on. The power was increased 5 V at a time until a visible transition into film boiling was observed as shown in Figure 2.3.
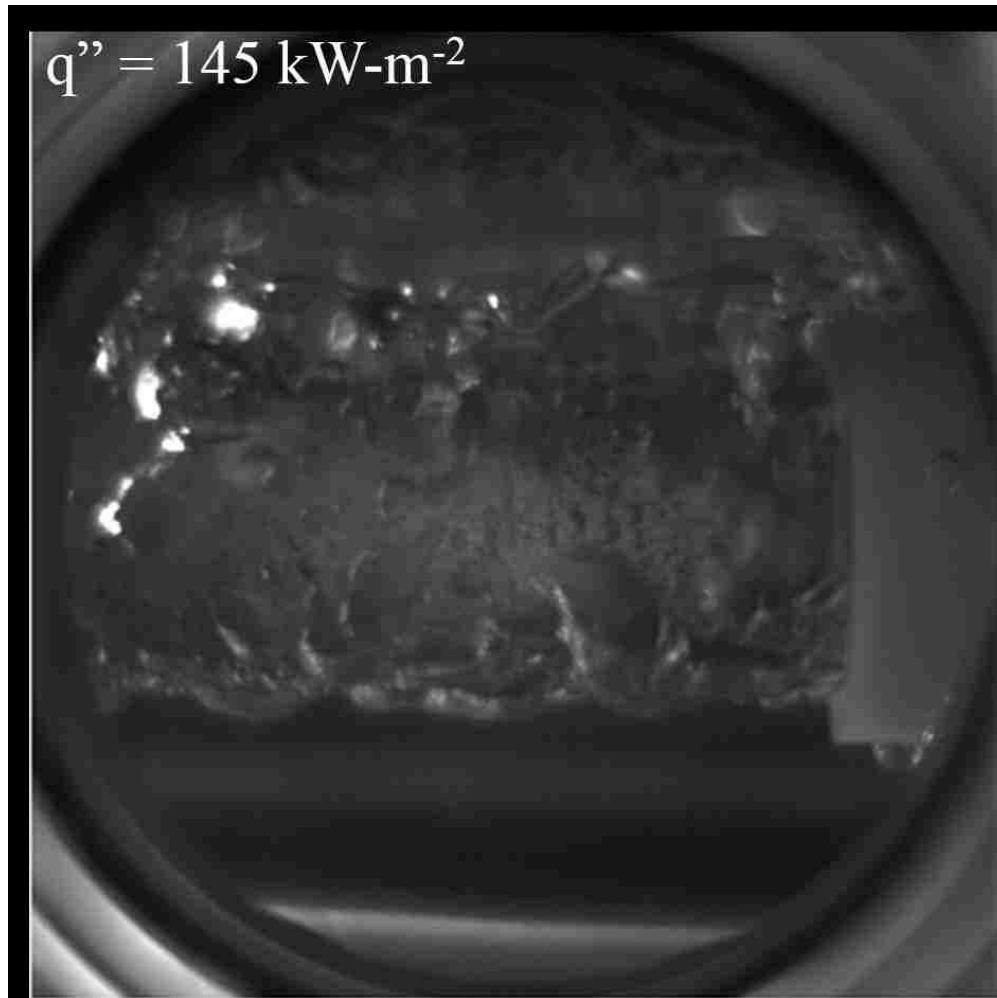
Figure 2.3: TiO₂ coated Al 6061 reaching transition boiling (working fluid is water, cylinder diameter is 19.1 mm)

Once transition boiling started to occur, the data collection ended and the critical heat flux is estimated based on the time the data collection stops. Temperature data from the thermocouples was gathered in separate sheets (1 sheet at each voltage) using the PersonalDAQ software and Microsoft Excel.

2.3. Data reduction

The power input from the Agilent Technologies DC power supply to the McMaster-Carr High-Temperature cartridge heater is estimated using Ohm's Law as seen in Equation (2.1). By dividing the power input by the area of the sample, the heat flux is calculated, as seen in Equation (2.2).

$$Q = VI \tag{2.1}$$

$$q'' = \frac{Q}{A} \tag{2.2}$$

The Q represents the total heat applied to the heater in kW, V is the voltage applied to the heater in V, I is current applied to the heater in A, A is area of the boiling surface in m^2, and q'' is heat flux in kW/m^2.

To accurately plot the pool boiling curve, the temperature readings from the thermocouples needed to be modified to reflect the temperature on the surface of the substrate. Figure 2.4 outlines the location of the power source input, the location of the thermocouples recording the temperature data, and the surface. Four thermocouples are placed in the sample so that the temperature data can be acquired from the top, left, right, and bottom of the sample. The average of these temperatures is used to find the wall superheat for the pool boiling plots against heat flux.
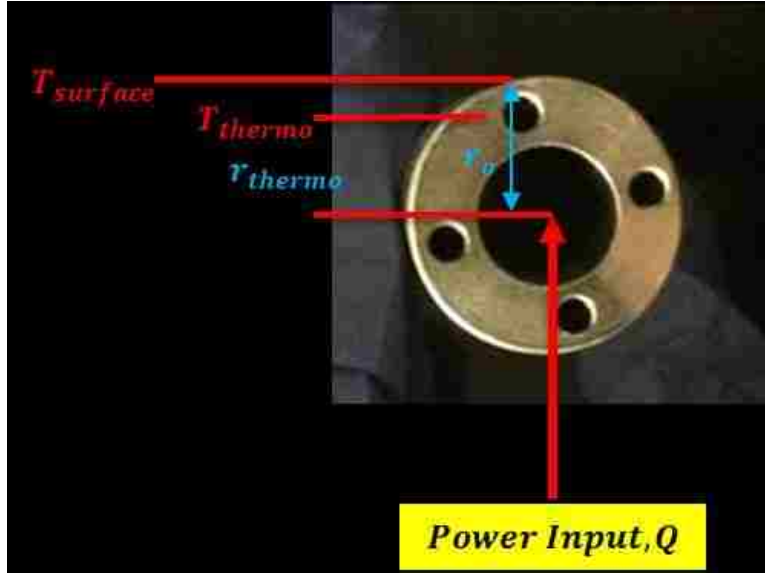
Figure 2.4: Image of aluminum 6061 heater sample outlining placement of power input and thermocouples

To find the temperature of the surface, a 1-D heat conduction equation is applied in the radial direction. This yields Equation (2.3).

$$T_{surface} = T_{thermo} - \frac{Q}{2\pi L}\left[\frac{ln(r_o) - ln(r_{thermo})}{k}\right] \qquad \textbf{(2.3)}$$

In Equation (2.3), $T_{surface}$ is the temperature of the surface, T_{thermo} is the temperature read by the thermocouple, L is length of the rod, r_o is the total radius of the cylinder, r_{thermo} is the distance between the center and center of the thermocouple, and k is thermal conductivity of the boiling surface.

To account for the total heat loss, the difference between the wall temperature and ambient temperature was divided by thermal resistance as shown in equation (2.4):

$$Q_{loss} = \frac{T_{wall} - T_{ambient}}{R} \qquad \textbf{(2.4)}$$

where Q_{loss} is heat lost in the system, T_{wall} is the temperature on the wall, and $T_{ambient}$ is the temperature of the surrounding environment. This resulted in the estimated heat loss shown in Table 1. The system was losing about 3 W of heat during the duration of the data collection, this

yields a higher impact on the data at lower heat inputs in this system. Heat loss gradually increases as the power input goes up; however, percentage loss decreases as the heat input goes up.

Table 1: Estimation of Heat Loss

Estimation of Heat Loss						
V	A	Q_{in} (W)	T (°C)	Q_{loss} (W)	$Q_{in, net}$ (W)	Percentage Lost
20.8	0.52	10.8	76.8	2.96	7.86	27.4
30.4	0.76	23.2	78.5	3.02	20.2	13.0
40.2	1.01	40.5	79.5	3.06	37.4	7.57
49.9	1.25	62.4	80.5	3.10	59.3	4.97
59.6	1.49	89.0	84.8	3.27	85.8	3.67
64.0	1.60	102.3	86.1	3.32	99.0	3.24
69.6	1.74	121.0	86.5	3.33	117.6	2.76
75.4	1.88	141.5	88.1	3.39	138.1	2.40

2.4. Uncertainty analysis

Kline and McClintock's technique is used to estimate errors from the uncertainties generated by voltage, current, and area [14]. Equation (2.5) was used to determine the random error of heat flux.

$$\frac{\Delta_{q"}}{q"} = \sqrt{\left(\frac{\Delta_V}{V}\right)^2 + \left(\frac{\Delta_I}{I}\right)^2 + \left(\frac{\Delta_A}{A}\right)^2}$$

(2.5)

$\Delta_{q"}$ is the overall heat flux uncertainty, Δ_V, Δ_I, and Δ_A are voltage, current, and area uncertainties. The voltage and current uncertainties are generated by the power supply, and the area uncertainty can vary from polishing and coating. The voltage and current measurement accuracy of the power supply is 0.1% [15].

Systematic uncertainty of the results can come from the overall heat loss of the system and thermocouple readings due to uncertain amount of thermal paste applied to the type T

thermocouples. The type T thermocouples have an estimated standard error of $\pm1.0\degree$C or 0.75%, whichever is greater [16]. The uncertainties in the experiment are further discussed in Chapter 3's uncertainty section.

2.5. Sample preparation of TiO2 coating

TiO_2 occurs in three different forms in nature: anatase, rutile, and brookite. Mo and Ching [17] did a study on the electronic and optical properties of anatase, rutile, and brookite TiO_2 and summarized that anatase contains 12 atoms per unit cell and rutile contains 6 atoms per unit cell, and Cromer and Herrington [18] conducted studies on the structure of anatase and rutile TiO_2 to find the lattice constants and the distances of the Ti-O bonds. The crystal structures of the anatase and rutile TiO_2 is tetragonal, whereas the brookite TiO_2 is orthorhombic. The anatase and rutile structures can be created in a lab setting; however, this is harder with brookite and is almost exclusively a naturally occurring crystal structure of TiO_2. The rutile structure is closer to a cubic structure (c/a = 0.65) whereas anatase c/a value is 2.51 as explained in a study done by Srivastava et al. [19].
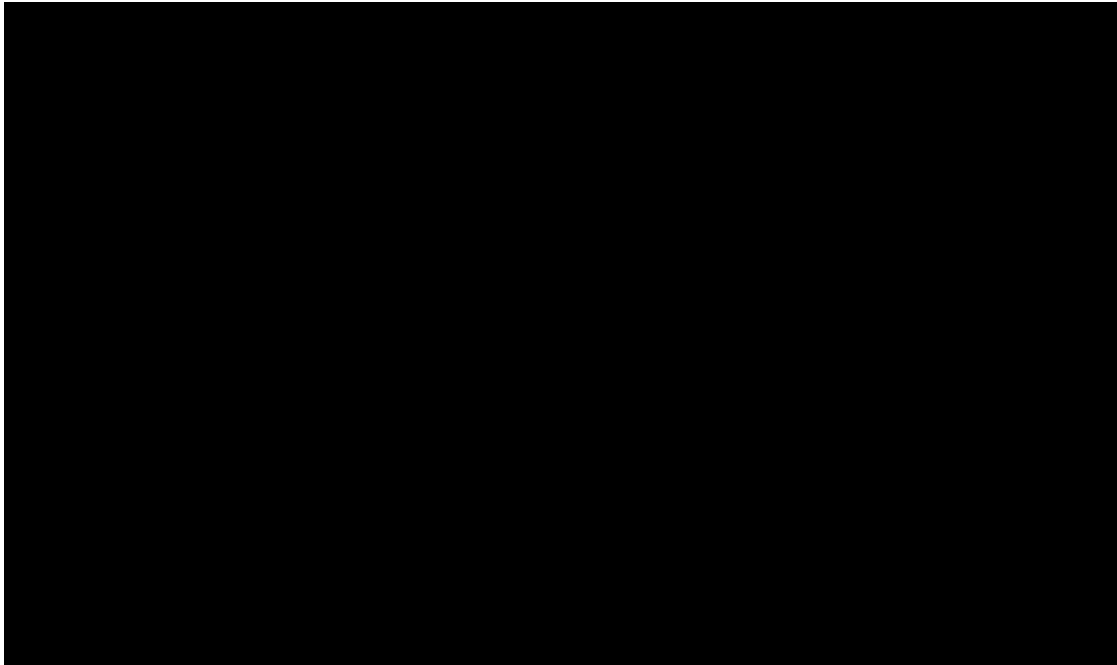
Figure 2.5: Anatase and rutile TiO₂ cells marked with 101 and 100 planes

Anatase TiO$_2$ is a photocatalyst, and when exposed to ultraviolet light with wavelengths shorter than 380 nm, it induces a photocatalytic reaction and contains strong oxidizing power. One significant property it gains is self-cleaning due to becoming super oleophobic (a common attribute of a surface that is super-hydrophilic), so the surface will absorb water, but reject oils. Previous studies from Takata [11] have shown that irradiated anatase TiO$_2$ yielded an increase in critical heat flux and better heat transfer during nucleate pool boiling. Without the ultraviolet light exposure, however, TiO$_2$ is still an interesting material for pool boiling because of its natural hydrophilicity. The TiO$_2$ coating process was based on to the coating process conducted in the study by Wu et al. [7]. Some of the results of their study can be attributed to the 101 crystal structure of TiO$_2$, as seen in Figure 2.6, since it already makes the substrate hydrophilic without the UV treatment.
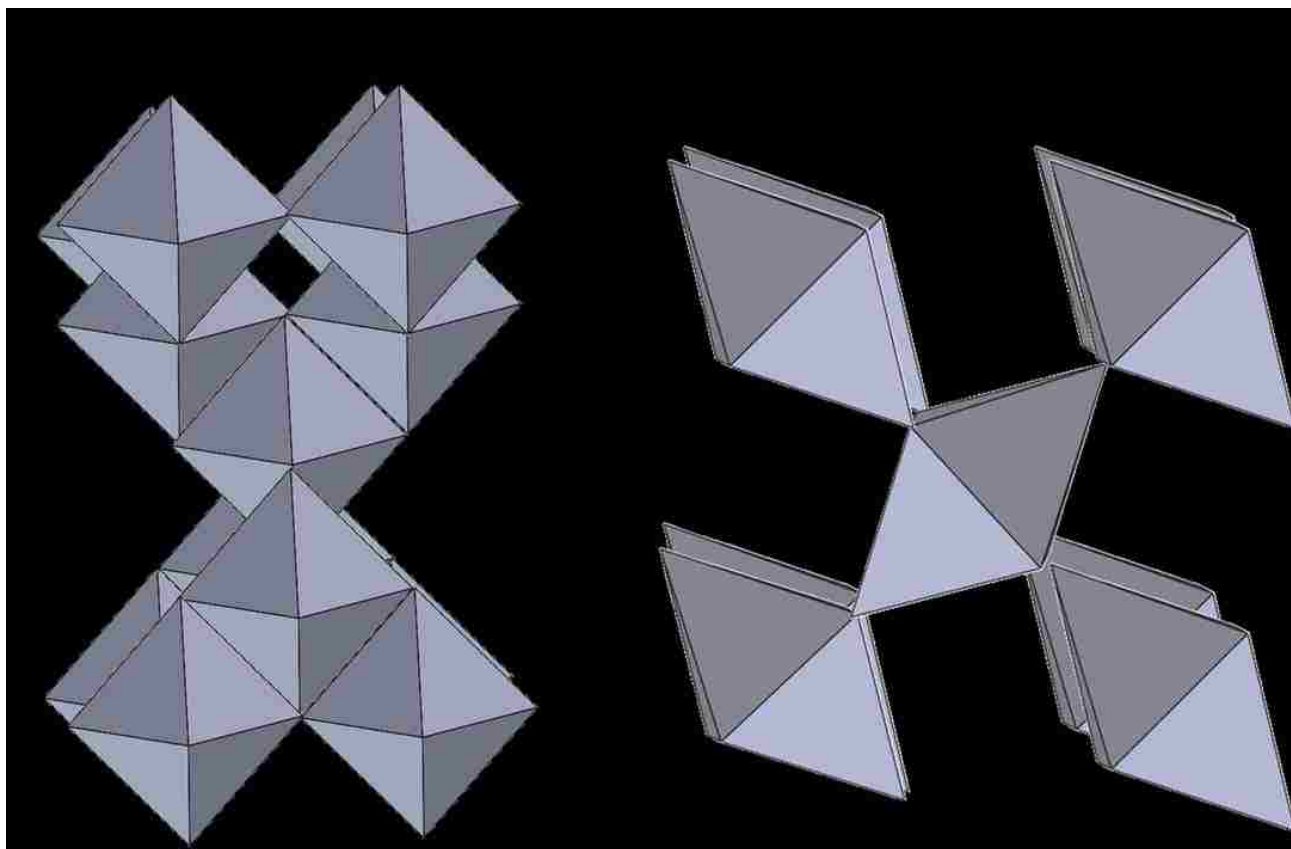
Figure 2.6: TiO2 crystal structures: anatase formation (left) and rutile formation (right)

To apply the TiO_2 coating on to the Al 6061 sample, two methods were used. The first

method was slightly difficult because the geometry of the samples was cylindrical, unlike Wu's

[8] square copper samples. Wu's procedures were followed verbatim. The first step was to polish

the Al 6061 sample with high grit sand paper. The sample is cleaned using acetone and rinsed

with DI water. The acetone is to rinse out any deposits and dirt on the sample. Then, an aqueous

solution was prepared with 1% weight anatase TiO_2 and 99% weight ethanol. Wu reports that

when the ethanol evaporated, 10 nm sized particles deposited into the surface. Drops of the

solution were then applied evenly throughout the sample and heated at 200°C in an oven for 30

minutes. This was repeated through the four different sides of the sample.

A second method was used involved the application of the base coating of NeverWet[TM]

before applying the solution evenly through the sample. NeverWet[TM] is used to repel moisture on

products and it works by applying two layers of coating – a base coat and a top coat. The base coat has a hydrocarbon resin and has naphtha and ester solvents and the top coat has acetone solvents [20]. The base coat is used in this method. This method was used because it provides the TiO_2 with an agent to help latch on to the sample and it would be helpful to observe if the TiO_2 crystal structure, or if overall wettability would have a bigger factor in generating better heat transfer in pool boiling. After the sample was prepared, contact angles were taken to verify uniformity and Scanning Electron Microscope (SEM) images were taken as seen in Figure 2.7 and Figure 2.8.
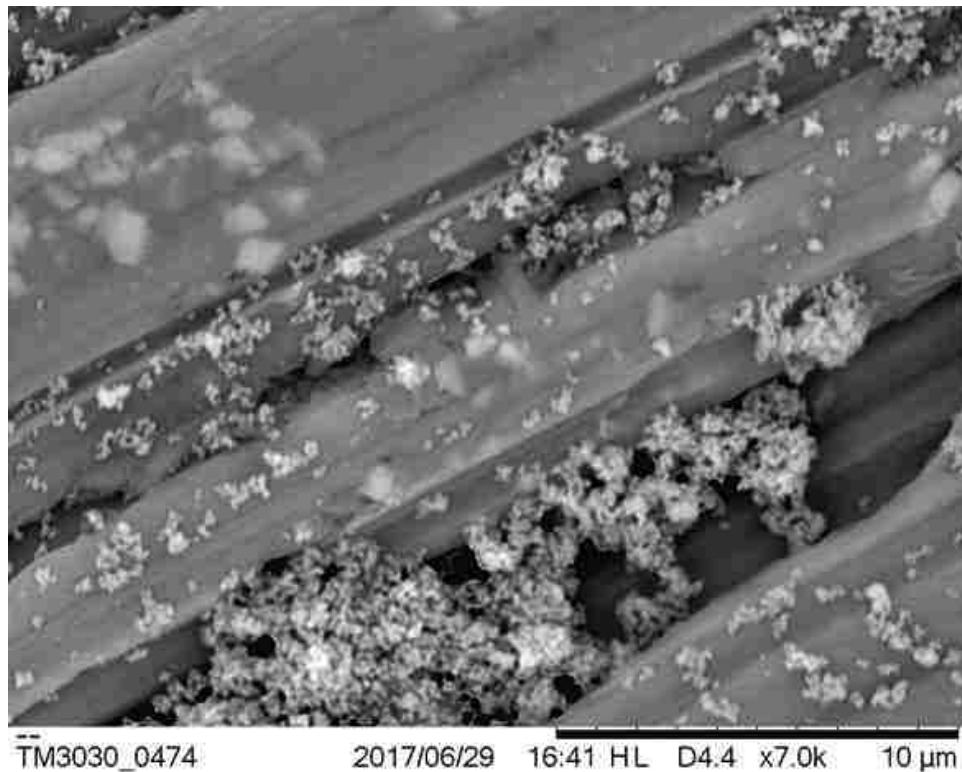
Figure 2.7: SEM image of Al 6061 surface with TiO₂ coating (x7000 zoom)
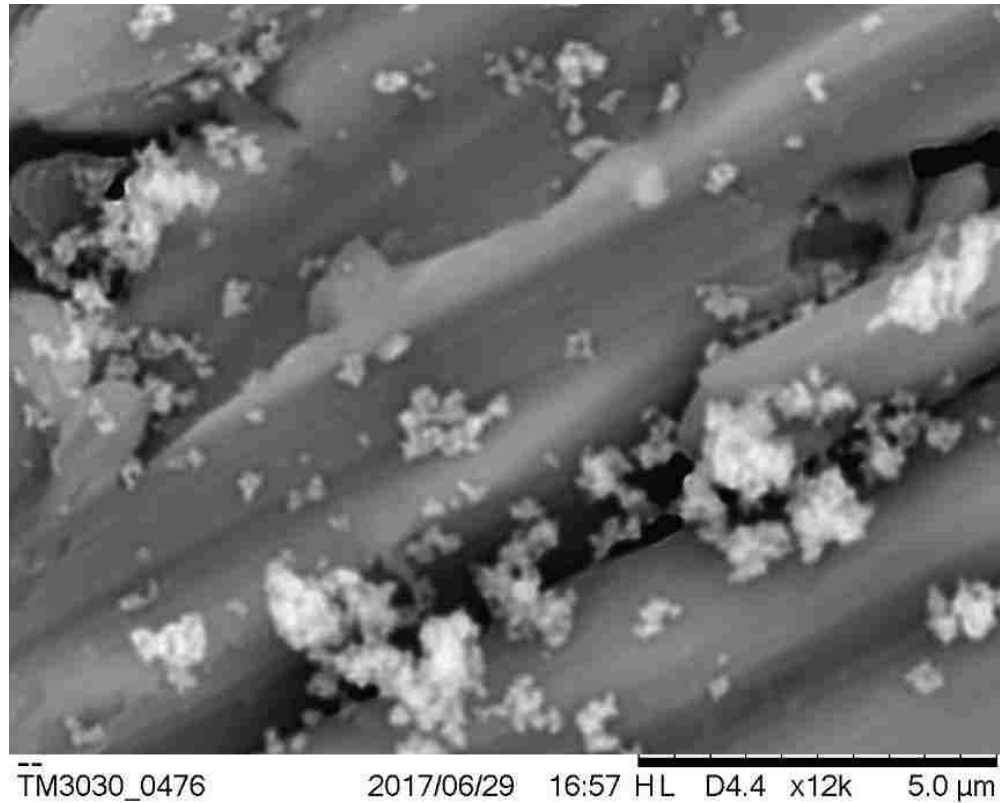
Figure 2.8: SEM image of Al 6061 surface with TiO2 coating (x12000 zoom)

The TiO_2 crystals in Figure 2.7 and Figure 2.8 seem similar to the 101 structure seen in Figure 2.6. These crystal structures appear to have an impact on the wettability of the working fluid and the surface of the substrate. The contact angle information supports this and can be seen in the next section.

2.6. Contact angle and surface profile of TiO2 coated Aluminum 6061

The wettability of the working fluid to the surface has an impact on heat transfer in condensing and boiling. The wettability can be determined by obtaining the contact angle between the surface and liquid droplet. For water, contact angles less than 90 degrees indicate that the surface is hydrophilic and the droplet will be spread out through the surface, whereas

19

contact angles of greater than 90 degrees indicate that the surface is hydrophobic and the droplets will be more spherical.
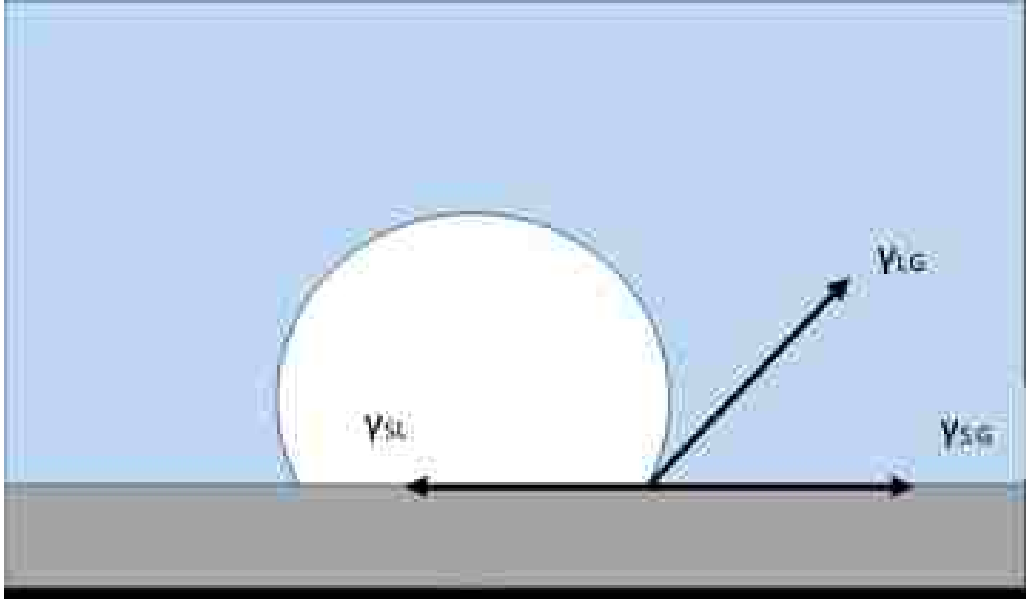
Figure 2.9: Surface tension force balance of a liquid droplet on a surface

The system in Figure 2.9 shows a liquid droplet and the surface tensions (liquid-gas, solid-gas, and solid-liquid). Cheng et al. [21] discusses theoretical considerations of the three surface tensions that govern the force balance of the droplet. Young's equation balances these forces as given by Equation (2.6):

$$\gamma_{LG} \cos \theta = \gamma_{SG} + \gamma_{SL} \tag{2.6}$$

where γ_{LG} is the surface tension of the liquid-gas interface, γ_{SG} is the surface tension of the solid-gas interface, and γ_{SL} is the surface tension of the solid-liquid interface. Furthermore, Lin et al. [22] discusses the role of interfacial tensions and the detachment of air bubbles in flat surfaces (emerging and detached bubbles) and tilted plains (emerging bubble, sliding bubble, and detached bubble) and summarizes the force components of bubble attachment and detachment in the following equations:

$$f_1 = \pi\phi(\gamma \sin\theta + f_b \cos\theta) \tag{2.7}$$

$$f_2 = \pi\phi\gamma \cos\theta \tag{2.8}$$

$$f_3 = \pi\phi f_b \sin\theta \tag{2.9}$$

$$f_4 = B \tag{2.10}$$

$$f_5 = 0 \tag{2.11}$$

where B is the buoyancy force, θ is the dynamic contact angle, $\pi\phi$ is the circumference of the circular contact base of a bubble on the surface, γ is interfacial tension, f_b is force from the gas pressure, f_1 is the attaching force, f_2 is the bubble closing force, f_3 is the base expanding force, f_4 is the bubble detaching force, and f_5 is the bubble drifting force. The closing force and expanding force are compared to determine if the circular contact base $\pi\phi$ is expanding ($f_3 > f_2$) or contracting ($f_3 < f_2$) and the bubble detaching force must be greater than the bubble attaching force ($f_4 > f_1$) for bubble detachment to occur. For hydrophilic surfaces, interfacial tension affects the bubble closing force (increasing the likelihood of the bubble base contracting) and does not have much of an impact of the bubble attaching force [because of the low contact angle based on Equation (2.7)]. This means that on a hydrophilic heated surface, it is likely that the bubble departure frequency would be higher and the bubble diameter would be smaller than it would be on a hydrophobic heated surface. The implications of this is that a very hydrophilic surface should yield better heat transfer in pool boiling than it would on a surface that has a contact angle of ~90°.
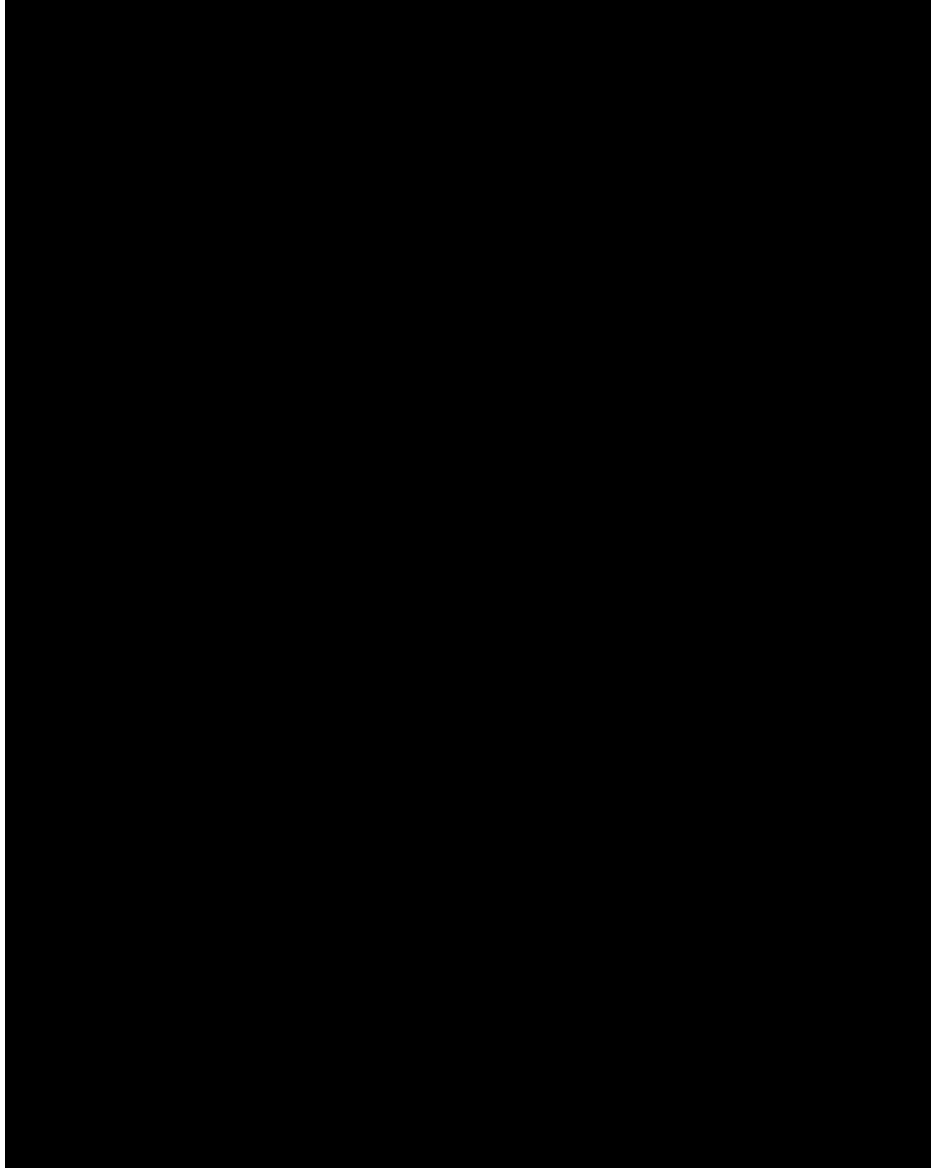
Figure 2.10: Diagram of the force balance of a bubble on a tilted surface

Lin et al. [22] summarized the forces of the bubble as follows in Equations (12-14):

$$f_1 = \pi\phi(\gamma \sin\theta + f_b \cos\theta)\cos\alpha \qquad (2.12)$$

$$f_4 = B\cos\alpha \qquad (2.13)$$

$$f_5 = B\sin\alpha \qquad (2.14)$$

where f_1 is the attaching force, f_4 is the bubble detaching force, and f_5 is the bubble drifting force, and α is the angle of the tilted surface. The bubble closing and expanding force observe no change and bubble drifting force becomes a factor. Unlike with a flat, horizontal heater, the bubble drifting force can be observed on a cylindrical heater through the sliding of the bubble. The bubble slides from the bottom of the sample and drifts up the side and eventually detaches. In his PhD dissertation, Zhang [8] discusses the increasing amount of impact water contact angle hysteresis has as the angle of a tilted surface increases due to hydrodynamic pressure differences. For a cylindrical heater, the bubbles detaching force coincides with buoyancy and there is no drifting force, at the sides, the water contact angle hysteresis has a larger impact and distorts the bubble, and at the bottom, the drifting force is at the maximum value.
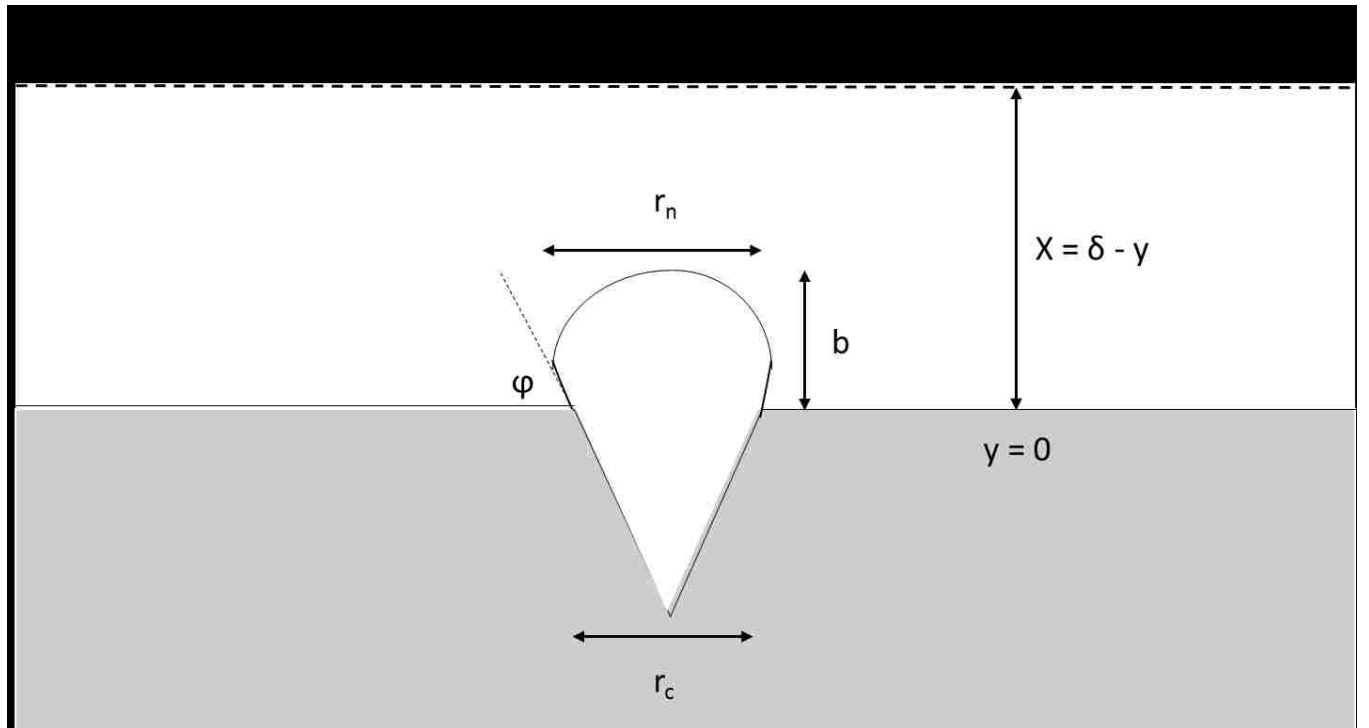
Figure 2.11: Variables and boundaries of a bubble formed on a cavity

Figure 2.11 displays bubble nucleation on a cavity. Mathematically, the 1-D transient conduction process can be described in the following partial differential equation:

$$\frac{\partial \theta}{\partial t} = \alpha \left(\frac{\partial^2 \theta}{\partial x^2} \right) \tag{2.15}$$

where θ is the temperature, x is the spatial variable, and t is the time variable. The assumptions for solving equation (2.15) are the following: a small bubble embryo exists on the cavity mouth, the temperature field within the thermal boundary, δ, is constant, and for $y > \delta$, heat transfer by molecular diffusion, and for $y > \delta$, turbulent transport results in uniform temperature. The temperature profile of the bubble can be derived using the Young-Laplace equation and Clausius-Clapeyron equation as the governing equations:

$$\Delta p = -\sigma \bar{\nabla} \cdot \hat{n} \tag{2.16}$$
$$ds = \left(\frac{\partial s}{\partial v} \right)_T dv + \left(\frac{\partial s}{\partial T} \right)_V dT \tag{2.17}$$

where Δp is the pressure difference, σ is surface tension, $\hat{n}$ is the unit normal pointing out of the surface. Because of surface wetting of the cavities, Δp is assumed to be the equivalent to the capillary pressure in a tube, in which case the Young-Laplace equation can be re-written as:

$$\Delta p = \frac{2\sigma}{r_c} \tag{2.18}$$

where r_c is the radius of the cavity in the surface. This is because the cavities are small enough to be assumed a tube. Next, $\left(\frac{\partial s}{\partial T} \right)_V dT$ term in Equation (2.17) is assumed to be zero because of constant temperature and pressure in a closed system during phase change. Applying Maxwell's relation and the assumption to Equation (2.17) yields:

$$ds = \left(\frac{\partial P}{\partial T}\right)_V dv \qquad (2.19)$$

Since P and T are constant, the derivative of pressure does not change with respect to temperature; therefore, the partial derivative of specific entropy may be changed to a total derivative, Equation (2.20) and integrating it from initial phase α to final phase β, yields Equation (2.21):

$$ds = \frac{dP}{dT} dv \qquad (2.20)$$

$$\frac{dP}{dT} = \frac{\Delta s}{\Delta v} \qquad (2.21)$$

where $\Delta s = s_\beta - s_\alpha$ (the change in entropy from initial phase α to final phase β) and $\Delta v = v_\beta - v_\alpha$ (the change in specific volume from initial phase α to final phase β). Next, using the first law of thermodynamic, given constant pressure and temperature, shown in Equation (2.22) and the definition of enthalpy, Equation (2.23), Equation (2.24) can be derived by combining Equation (2.22) to Equation (2.23):

$$du = T\,ds - P\,dv \qquad (2.22)$$

$$dh = du + P\,dv \qquad (2.23)$$

$$dh = T\,ds \qquad (2.24)$$

Rearranging Equation (2.24) and applying Equation (2.21) to (2.24) yields:

$$\Delta p \cong \frac{h_{lv}\Delta T}{T_{sat}\Delta V} \qquad (2.25)$$

where h_{lv} is the latent heat of vaporization in $\frac{J}{kg}$. By combining equations (2.18) and (2.25), the following relation is formed:

$$\Delta p = \frac{2\sigma}{r_c} = \frac{h_{lv}\Delta T}{T_{sat}v} \tag{2.26}$$

Then, solving for ΔT yields:

$$\Delta T = \frac{2\sigma T_{sat}v}{h_{lv}r_c} \tag{2.27}$$

Finally, by simplifying Equation (2.27), a relationship between the bubble wall superheat and latent heat of vaporization, cavity radius, and vapor density is formed in Equation (2.28):

$$\Delta T = \theta_w - \theta_{sat} = \frac{2\sigma T_{sat}}{h_{lv}\rho_v r_c} \tag{2.28}$$

where $\theta_w - \theta_{sat}$ is the bubble wall superheat in K, ρ_v is the vapor density in $\frac{kg}{m^3}$, and r_n is the radius of the surface cavity m. Equation (2.28) provides insight to the wall superheat temperature for the bubbles forming on the surface. This information is relevant when attempting to predict the radii range of nucleation site using Hsu's equation [23] – this is further discussed later in this section.

To find the contact angle of the sample surfaces, the KSV CAM 200 Goniometer was used (seen in Figure 2.12).
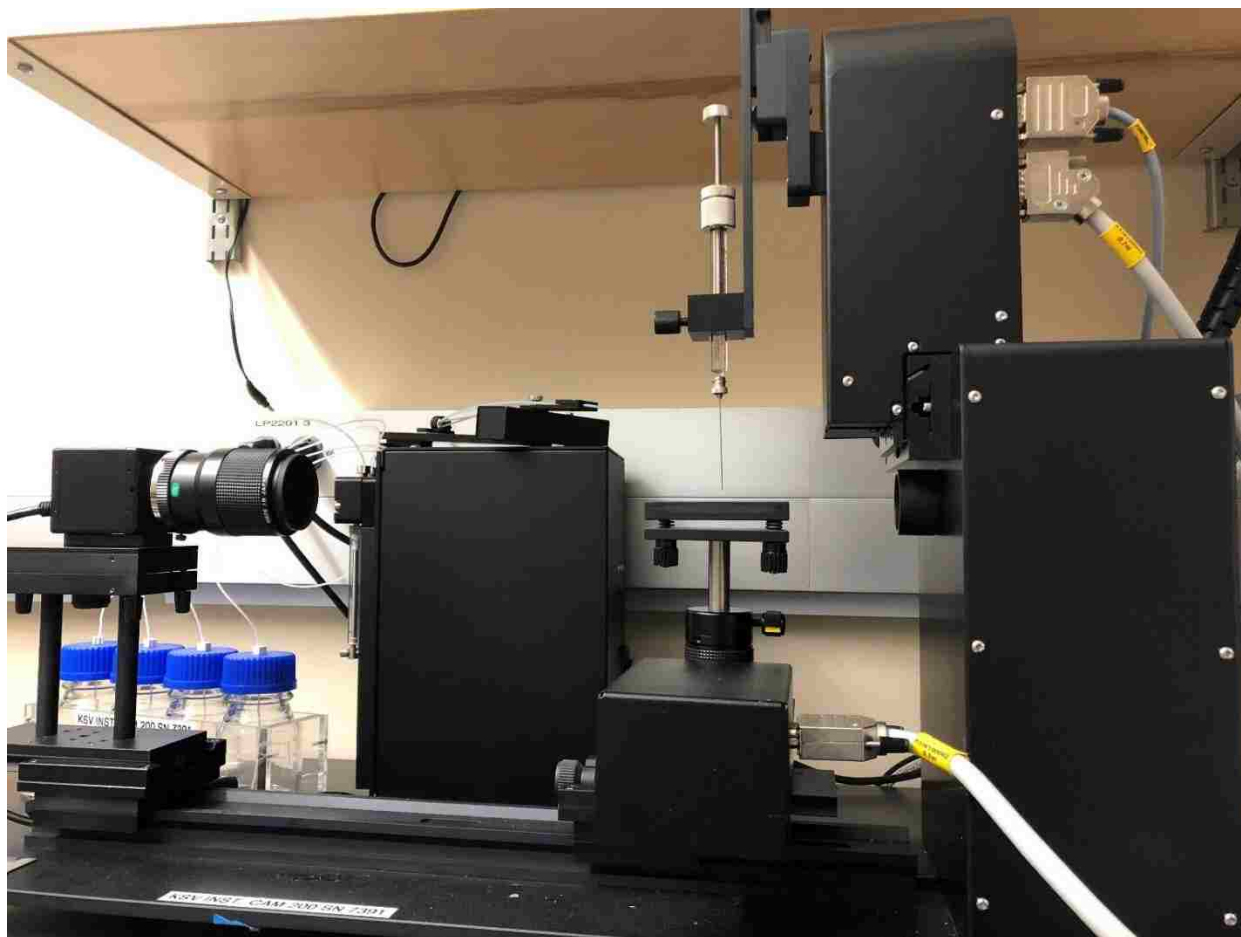
Figure 2.12: KSV CAM 200 Goniometer (Used for quantifying wettability)

The sessile drops application was used to determine the contact angles between the various

surfaces. Multiple trials were conducted to find a solid average and to ensure the coating in the

surfaces were even.

Figure 2.13: Water droplet on a plain Al 6061 surface; average contact angle: 81 °

The contact angle was found by distributing droplets throughout the sample to ensure

uniformity of the surface. Figure 2.13 shows the droplet on a plain Al 6061 surface. The contact

angle of the untreated surface was obtained to gain baseline data. The untreated Al 6061 surface

averaged an 81° contact angle and had a standard deviation of 2.16.

**Figure 2.14: Water droplet on TiO$_2$ coated Al 6061 with NeverWet; average contact angle:
65 °**

Figure 2.14 shows a droplet on a TiO$_2$ coated Al 6061 surface that was treated with

NeverWet^{TM}. The contact angle on this surface averaged a 65° contact angle and had a standard

deviation of 4.85. This impact in wettability may be attributed to the base coating of

NeverWet™.

Figure 2.15: Water droplet on a TiO2 coated Al 6061 surface; average contact angle: 15 °

Figure 2.15 shows a droplet on a TiO_2 coated Al 6061 surface. Comparing Figure 2.13, Figure

2.14, and Figure 2.15, it can be observed that the TiO_2 makes the surface significantly more

hydrophilic. The average contact angle of the surface was 15˚. The contact angle data set had a

standard deviation of 1.89.

The TiO_2 coated Al 6061 sample was observed using a VHX 100 optical microscope.

Using one of the features of the microscope, a surface profile was obtained in the observed area.

The surface profile can be seen in Figure 2.16.
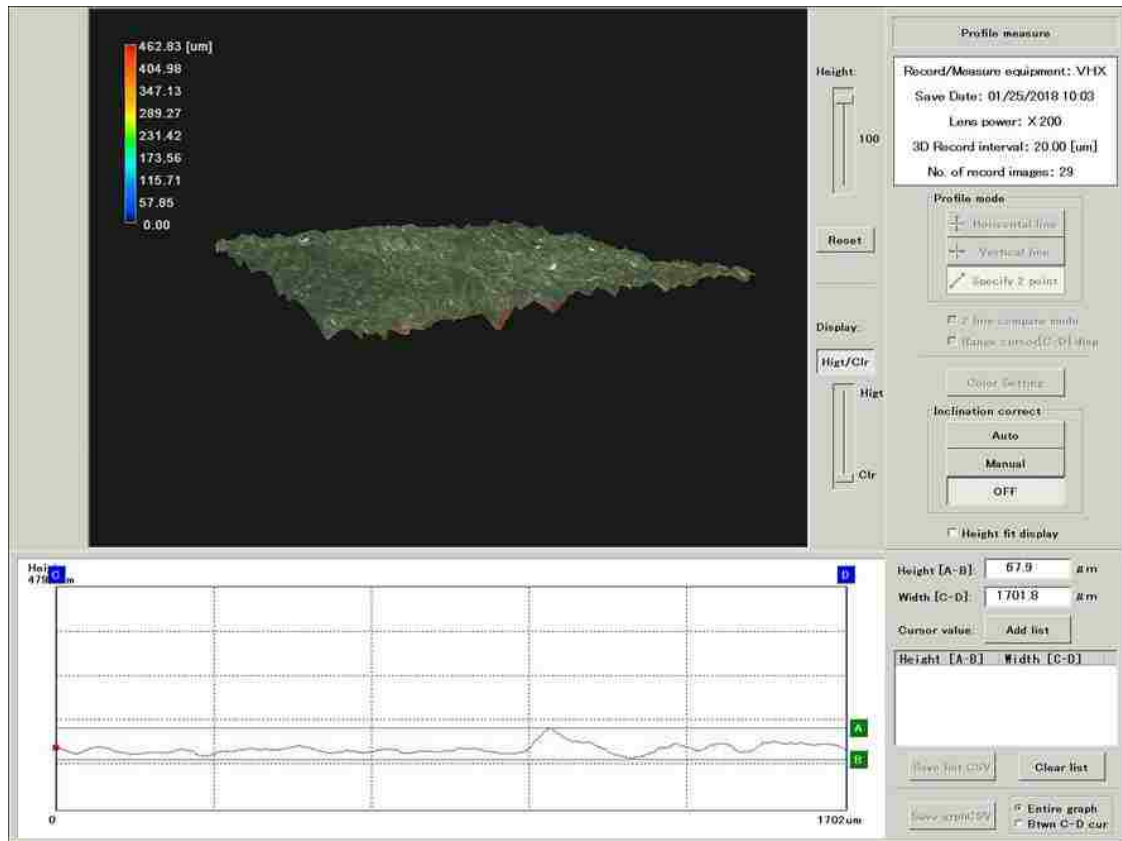
Figure 2.16: Optical microscope generated surface profile of TiO₂ coated Al 6061 substrate

Hsu [23] conducted a study on varying sizes of nucleation cavities and created a model

that showed the maximum and minimum sizes of effective cavities as functions of sub-cooling,

pressure, physical properties, and thickness of the thermal boundary layer. In his study, Hsu

concluded that sizes of active cavity sites are dependent on the limiting thickness of the thermal

layer, and for the nucleation site to be active, it must have a favorable geometry, the cavity must

be within the size range of the effect nucleation sites, and nearby cavities need to be within a

certain area of the site. Figure 2.16 provides a visualization of the surface and allows an

estimation of cavity information on the surface for comparison to Hsu's model, which correlates

cavity radii throughout the surface and the bubble temperature profiles. It also provides

information such as cavity depth (in this case, the software estimates the difference between the

highest and lowest points in that particular cross section to be 67.9 microns) through designated

cross sections of the sample and can give a general idea of the diameter of such cavities based on when the height of the sample comes back up. Hsu's model for relating cavity size range with the bubble temperature profile can be seen in Equation (2.29):

$$\begin{Bmatrix} r_{c,max} \\ r_{c,min} \end{Bmatrix} = \frac{\delta}{2C_1} \left[1 - \frac{\theta_{sat}}{\theta_w} \pm \sqrt{\left(1 - \frac{\theta_{sat}}{\theta_w}\right)^2 - \frac{8\sigma T_{sat} C_2}{\delta \theta_w h_{lv} \rho_v}} \right]$$

$$(2.29)$$

where r_c is the radius of the surface cavities, δ is the limiting thermal boundary layer, θ is the bubble surface temperature, σ is the surface tension of the liquid with respect to vapor, h_{lv} is the latent heat of vaporization, ρ_v is the vapor density, and the C's are experimentally found constants. Equation (2.29) is used to help estimate where nucleation points may occur during pool boiling.

Chapter 3. Visualization and Data Collection of Pool Boiling on TiO$_2$ Coated Surface

Temperature data and heat flux data was gathered starting with a baseline set with plain Aluminum 6061 heaters. After a baseline pool boiling curve was established, an Al 6061 substrate was prepared with TiO$_2$ coating based on Wu's method and another substrate was prepared with TiO$_2$ coating using NeverWet^{TM} base coating as coupling agent as described in Chapter 2. The temperature data and heat flux data was collected and was used to generate pool boiling curves for comparison. Furthermore, high-speed camera videos were taken and processed to gather data and applied to an analytical model to compare with the experimental data. The purpose of this is to see if there is TiO$_2$ yields an improvement in heat transfer during nucleate pool boiling

3.1. Pool boiling on cylindrical aluminum 6061 surface for baseline data

A pool boiling curve was generated using the temperature data gathered from the thermocouples placed in the sample and pool boiling chamber and applying Equations (2.1) and (2.2) for the heat flux data and applying the heat conduction equation outlined in Equation (2.3) for the temperature data.
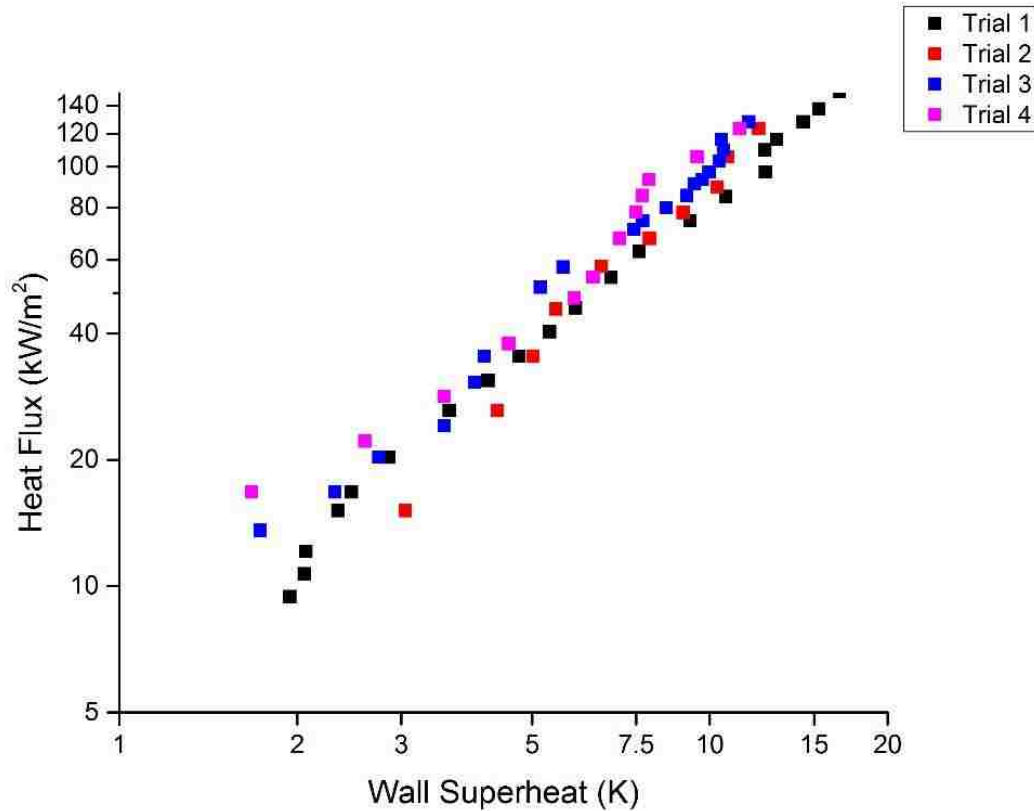
Figure 3.1: 4 baseline Al 6061 pool boiling curve by trial

This data was gathered to find a baseline boiling curve of Al 6061. The trials were consistent as seen in Figure 3.1.

Figure 3.2 shows the pool boiling curve data obtained compared with cylindrical plain Al 6061 pool boiling curve data published by two different investigators: Bhuiya [24] and Zhang [8]. There was little overall discrepancy between the three sets of data – Zhang's data appears to show the greatest discrepancy in pool boiling data. A few factors that may contribute to this discrepancy can range from variance in heat loss in the pool boiling chambers, differing sizes of the pool boiling chamber, or discrepancy in the experimental procedures for data collection.
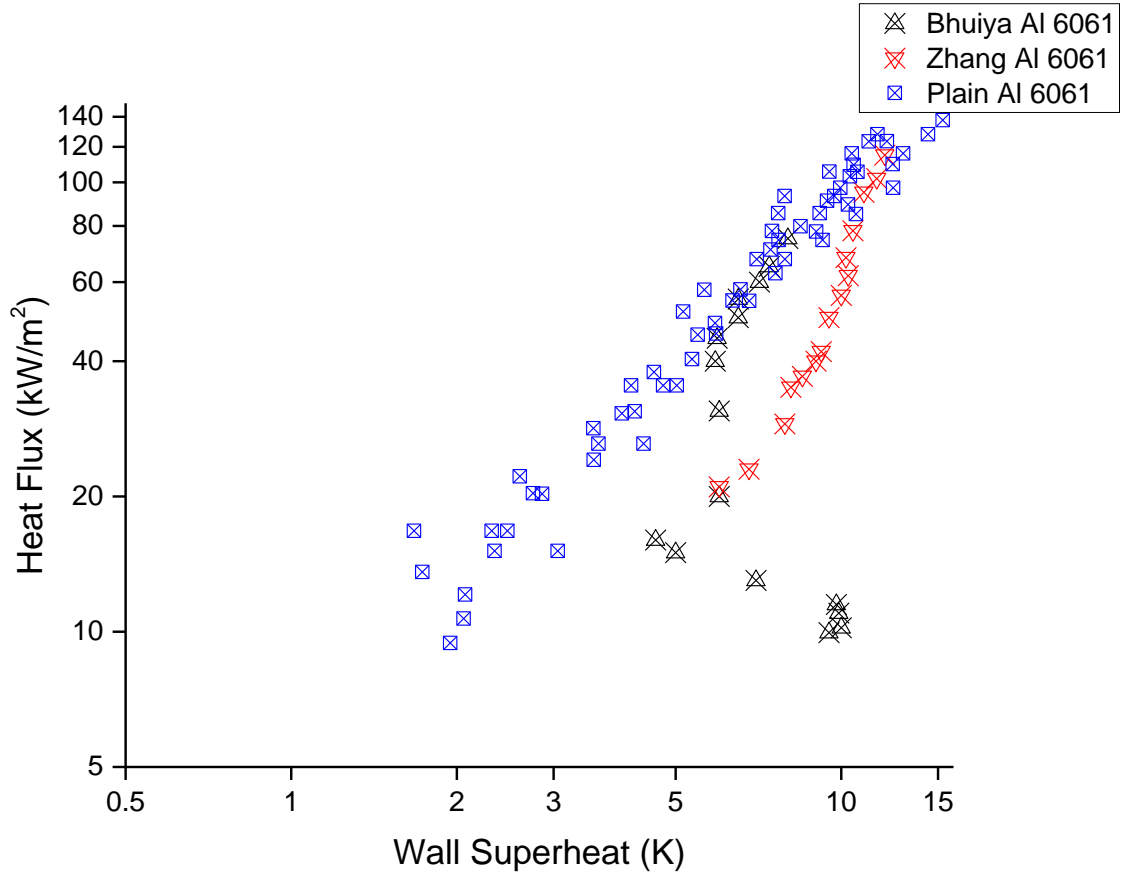
Figure 3.2: Baseline pool boiling curve compared with previously published data

The pool boiling curves of the individual trials of the two other samples can be found in Appendix A.

3.2. Pool boiling on TiO$_2$ coated Aluminum 6061 Surface

A pool boiling curve was generated for Al 6061 samples treated with TiO$_2$ with both methods. Al 6061 samples treated with NeverWet^{TM} are considered the "coupled sample" and the samples that were not treated with NeverWet^{TM} are considered the "uncoupled sample" in Figure 3.3. The pool boiling curve generated from the coupled sample trends closely with the plain Al 6061 sample, whereas the uncoupled sample yields a pool boiling curve of higher performance.
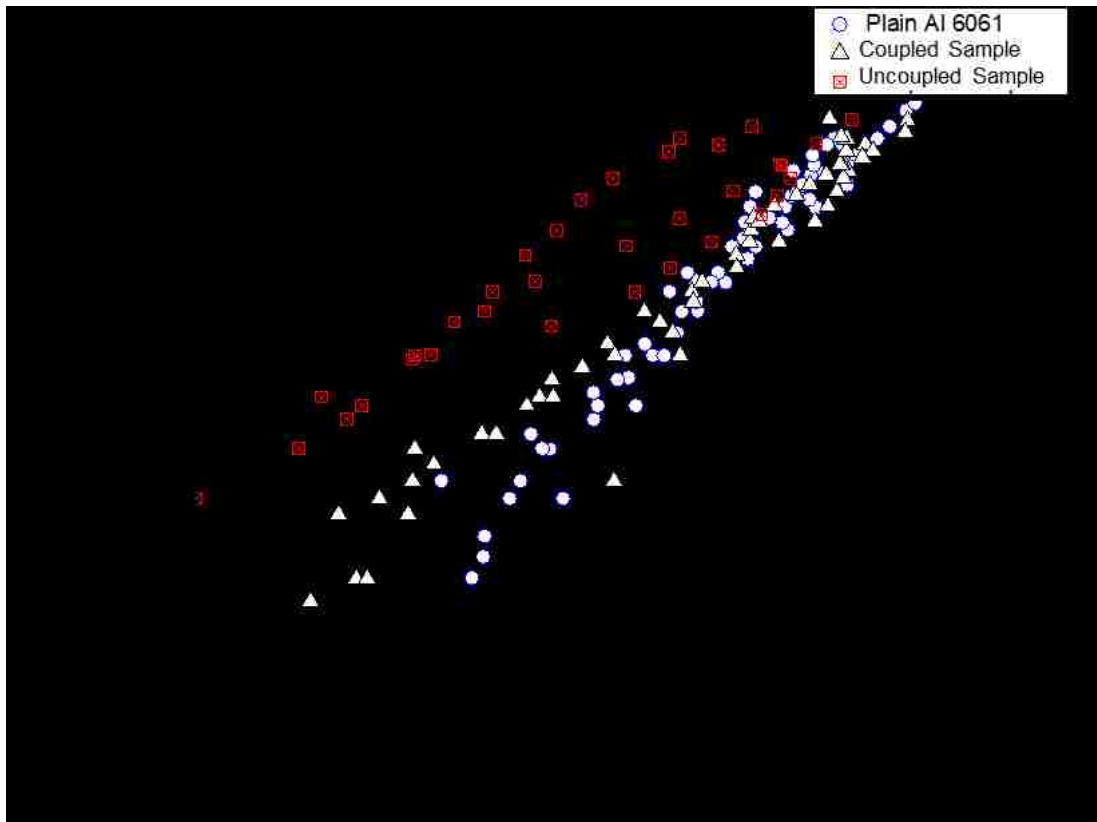
Figure 3.3: Pool boiling curve of baseline substrate vs both TiO₂ substrates

When looking at the data for the samples' wettability in water for the 3 samples, the data in

Figure 3.3 appears to coincide with the wettability of the samples because the contact angle of

the coupled sample and plain Al 6061 are relatively close and the uncoupled sample was

significantly more hydrophilic. This is probably because of the base coating used from

NeverWet™. Overall, the sample that was coupled with NeverWet™ performance did not show

much of an enhancement in boiling heat transfer, and even appears to drop off at high superheat

and heat flux. The uncoupled sample has an average contact angle (15˚) that is significantly

lower than the two other samples, so it appears the significant performance enhancement is

probably due to the wettability and roughness of the surface of the TiO₂ coating.

A hydrophilic surface with such a low contact angle should yield heat transfer enhancement through the help of bubble dynamics (faster departure frequency). This enhancement was also visually apparent with the higher bubble departure frequency and nucleation sites, and this is further discussed in the next section of the chapter.

3.3. Visualization comparison of pool boiling on plain Al 6061 surface and TiO$_2$ coated surfaces

The Phantom v4.3 high-speed camera was used to take footage of the pool boiling on the different surfaces. The camera can record up to 1,000 frames per second, produce videos that are 600 x 600 pixels, and is capable of continuous recording. The software, CineViewer was used to export the Phantom video files and convert them to .avi, .mp4, and .TIFF formats. This is a tool to acquire images to qualitatively compare and provide additional insight on pool boing of baseline and TiO$_2$ coated samples at varying heat fluxes.
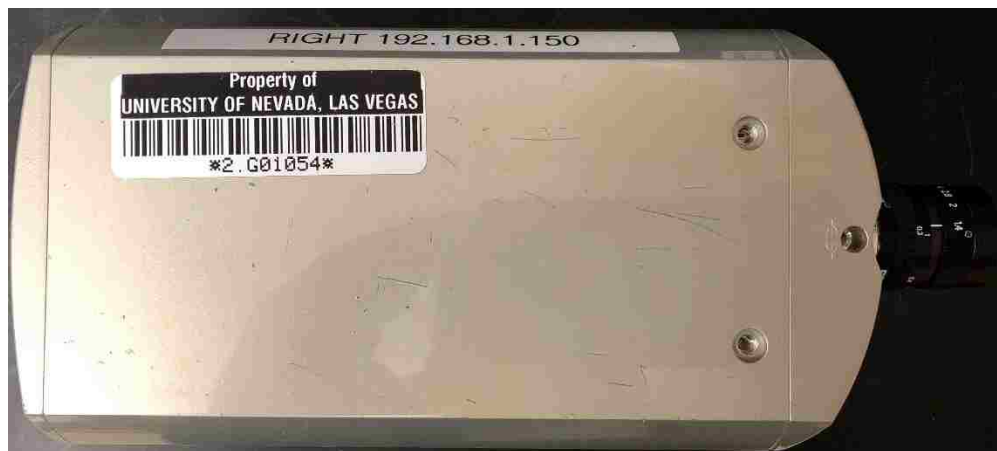
Figure 3.4: Phantom v4.3 High Speed Camera

Figure 3.5 shows images from the Phantom high-speed camera at varying heat fluxes (40, 60, and 120 kW-m^{-2}). This allowed for visual observation of the differences in bubble nucleation and departure between treated and untreated surfaces of Al 6061.
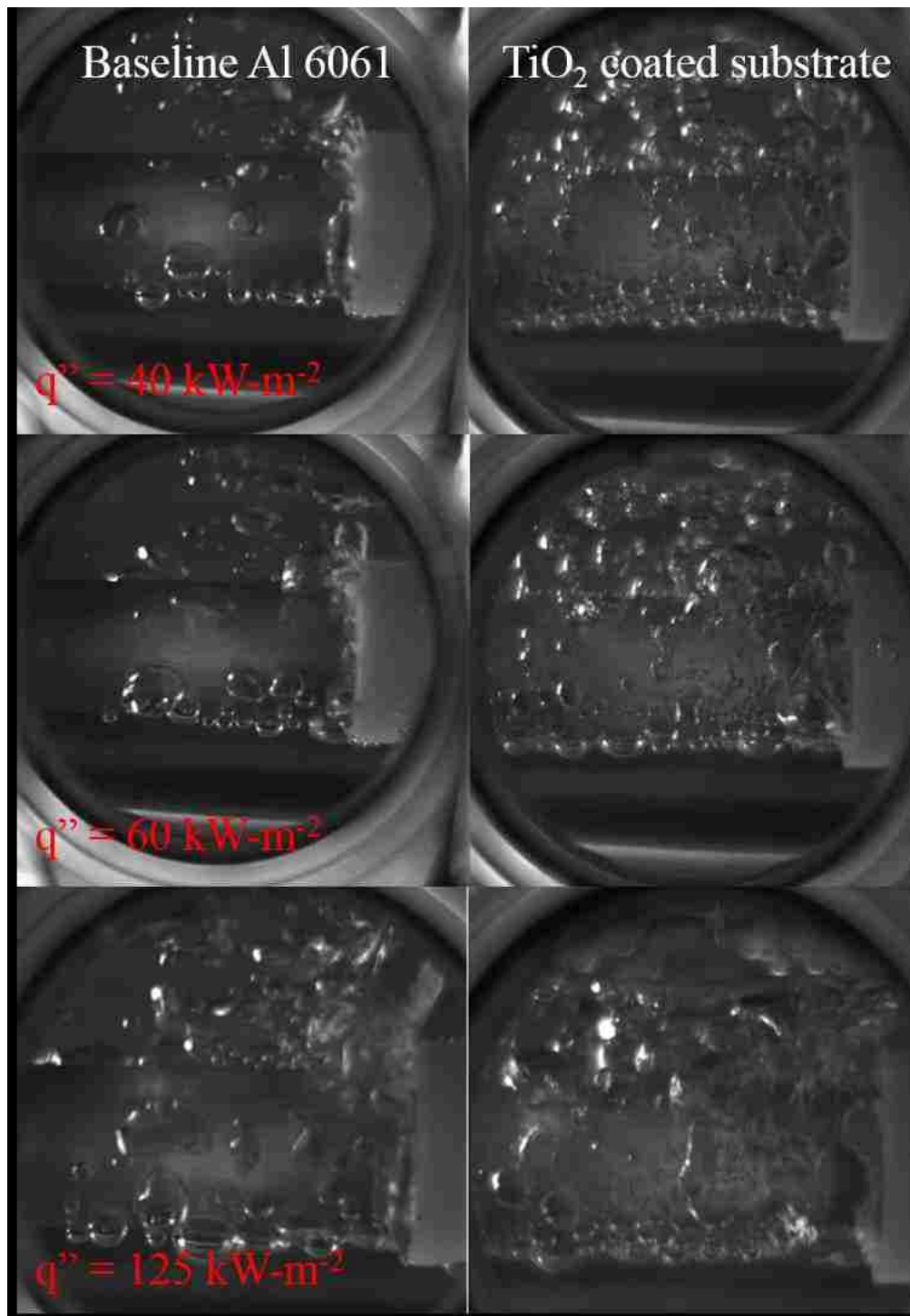
Figure 3.5: High speed camera images of pool boiling of baseline and TiO₂ coated sample at varying heat fluxes

Comparing the left and right images of Figure 3.5, a clear difference can be observed between plain Al 6061 samples and TiO$_2$ treated Al 6061 samples. The difference is very clear at a low heat flux of 40 kW/m^2, and at 120 kW/m^2 the treated sample appears to have a significant amount of active nucleation sites. Overall, the Al 6061 samples that were treated with TiO$_2$ have significantly more nucleation points and bubble departure frequencies throughout the surfaces of the sample. From an observational standpoint, it is easy to draw a conclusion that there is more heat transfer occurring (at least through liquid-vapor exchange) with the treated samples through these images. This can be verified by using the quantifiable information, such as active nucleation sites and bubble departure frequencies, plugging the information into a model (such as the vapor-exchange model proposed by Forster and Grief) and comparing the model with the experimental data shown in Figure 3.3 [2]. This is discussed later in the chapter in section 3.4.

A bubble detection code based on Kimme's [25] adaptation to the Circle Hough Transform (CHT) by Duda and Hart [26] was used to analyze the videos produced by the Phantom high-speed camera. This algorithm is computationally efficient and works by plotting an arc perpendicular to the edge orientation based on the given radius. A threshold is applied to an accumulator array to detect likely centers of circles in the specified area. A .TIFF file was exported from the camera and utilized to analyze the video frame by frame. Using the Kimmie's method, the code was used to detect different sized droplets based on the gradient of the images in the video file. Recently, Naccarato [27] utilized Kimmie's algorithm and implemented it using functions available in the MATLAB Image Processing Toolbox [28] for his droplet detection method in his dropwise condensation experimentation. Naccarato modifies the code to be able to find circles of varying radii while masking previously detected circles because the original CHT cannot detect a wide range of circle of varying radii in one loop and repeated loops result in false

positive detections. Naccarato's new algorithm was adjusted to fit the needs of detecting bubbles for pool boiling. The first step of detection begins with using the Sobel operator [29] for edge detection. The Sobel operator works by taking the gradient of the image, *G*, and generating 3x3 filters in the x and y directions, G_x and G_y. The magnitude of the gradient can be found in Equation (3.1):

$$|G| = \sqrt{G_x^2 + G_y^2}$$ **(3.1)**

The areas in which the magnitude of the gradient is the highest is estimated to be where the edges of the image is.

Figure 3.6 shows a sample image of various colored circles detecting bubbles of sizes corresponding to the color through a given area of the sample. For example, a magenta circle would be used to trace a circle between 21 and 27 pixels and a yellow pixel would be used to trace a circle between 0 and 2 pixels in radii.

Figure 3.6: Image of bubble detection processed by MATLAB based on the CHT

Using the CHT algorithm on MATLAB, bubble counts were obtained by frame. Each

plot shows the bubble diameter size on the x-axis and the frame number of the video on the y-

axis, and the total bubble count at the diameter and frame on the z-axis, as seen in Figure 3.7.

More histogram data can be found in Appendix B.
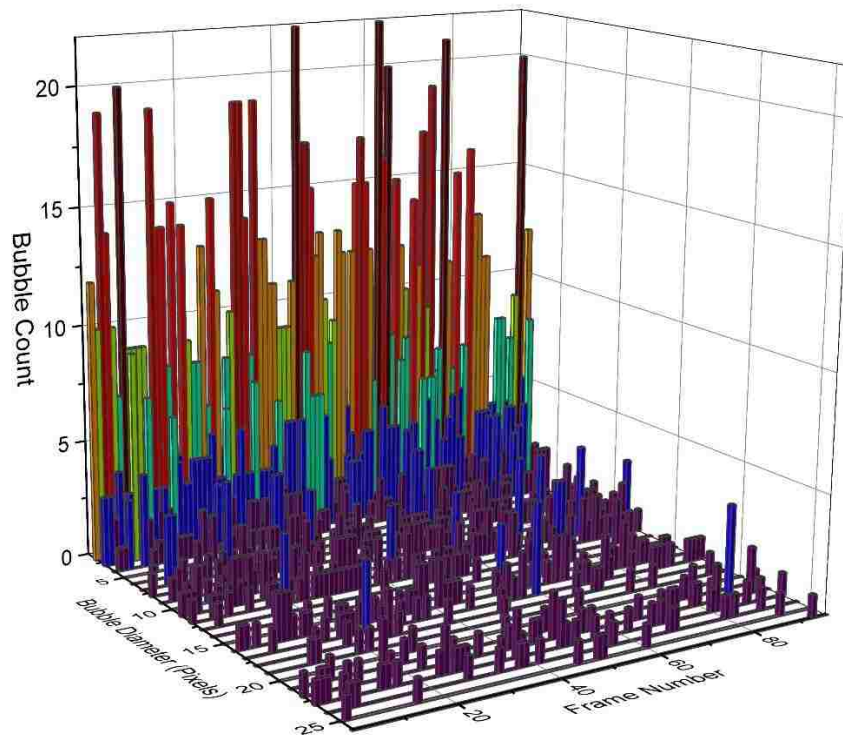
Figure 3.7: Histogram of bubble count by frame generated by MATLAB

The data found in the histogram was easily exportable to an excel file and the average

bubble counts at each bubble radii was found at each heat flux the videos were processed at.

This data was used to fill in variables of the models used in comparison with the experimental

data.

3.4. Comparison of experimental Data and current models

The experimental data was compared with the projected boiling curve of Forster and

Greif. Forster and Greif's vapor-liquid exchange model is shown in:

$$q'' = \rho_l c_{pl} \frac{2\pi}{3} R_{max}^3 \frac{1}{2} \Delta T f N_a \qquad \text{(3.2)}$$

where q'' is the heat flux, ρ_l is the liquid density, c_{pl} is the specific heat, R_{max} is the max radius

of the bubble, ΔT is the wall superheat, f is the departure frequency, and N_a is the active

nucleation site density. The bubble frequency and radius information was gathered from the

video files using MATLAB. Based on that data, a plot was generated and compared with the plot

generated from the experimental data as shown in Figure 3.8. There are a few variables that

impact the overall heat flux in this model: the max radii of the bubbles, the departure frequency,

and the number of active nucleation sites.
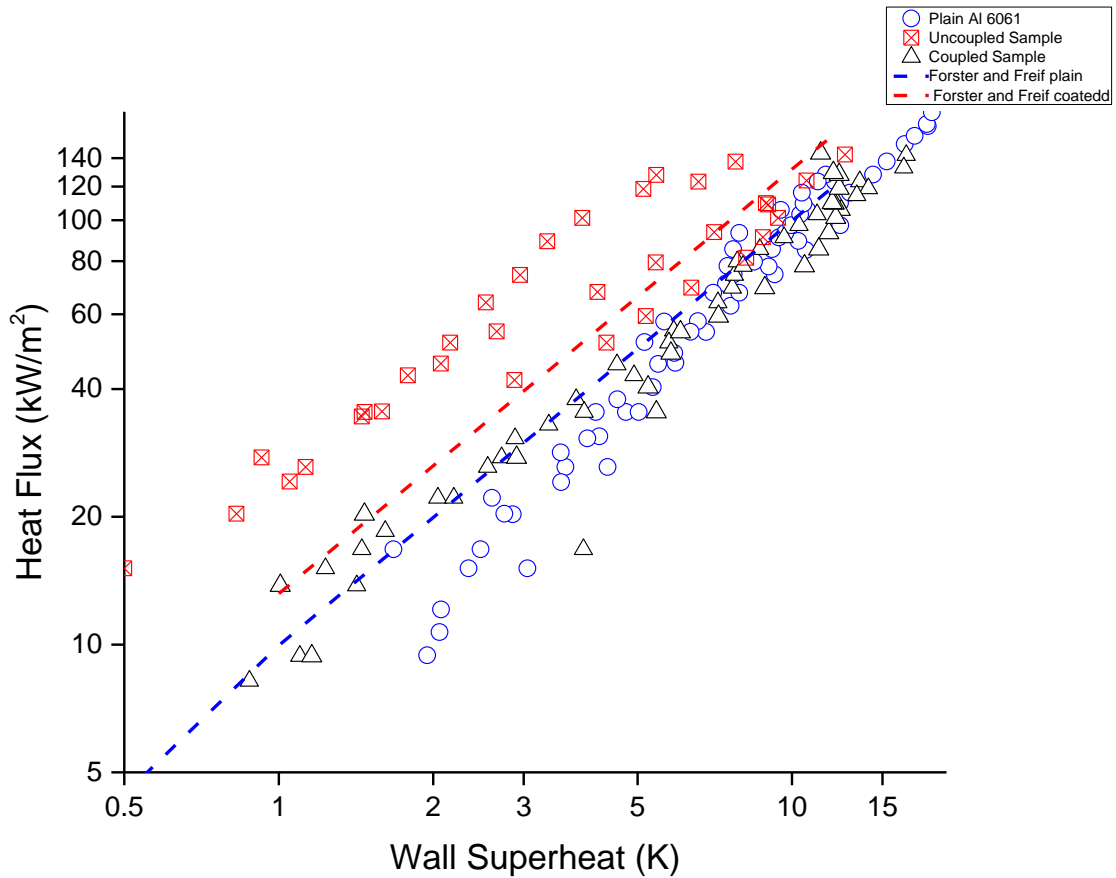
Figure 3.8: Comparison of experimental data with Forster and Freif's model

The Forster and Grief model [2] seemed to accurately follow the experimental data for the Plain Al 6061 towards higher superheat; however, the model seemed to slightly differ from the uncoupled version of the TiO_2 coated sample. This might be because the area processed on MATLAB only takes into account one side of the sample and with higher amounts of nucleation points, the model failed to keep up with the experimental data; the other side of the sample should be observed in future comparisons. Furthermore, bubble departure frequency had to be counted visually frame by frame, with frames being converted to seconds after achieving a raw count. This leads to some human error in this type of evaluation. In this specific case, active nucleation points seemed to be a dominating factor in the model generated pool boiling curve; this is evident in the numbers and video footage.

3.5. Uncertainty analysis

Uncertainty analysis was conducted using Equation (2.5) as discussed in section 2.4 [14]. The uncertainties for wall superheat and heat flux were found and tabulated.

Table 2: Heat flux uncertainty

Heat Flux Uncertainty								
Δv (V)	V (V)	Δi (A)	I (A)	Δa (m^2)	A (m^2)	q" (kW/m^2)	Δq" (kW/m^2)	% Uncertainty
0.042	20.8	0.001	0.520	0.00012	0.00115	9.44	0.99	5.24
0.050	24.9	0.001	0.625	0.00012	0.00115	13.6	1.42	5.24
0.055	27.7	0.001	0.694	0.00012	0.00115	16.8	1.76	5.24
0.061	30.5	0.002	0.764	0.00012	0.00115	20.3	2.13	5.24
0.066	33.2	0.002	0.833	0.00012	0.00115	24.1	2.52	5.24
0.075	37.4	0.002	0.938	0.00012	0.00115	30.6	3.20	5.24
0.080	40.2	0.002	1.007	0.00012	0.00115	35.3	3.70	5.24
0.097	48.6	0.002	1.216	0.00012	0.00115	51.6	5.40	5.24
0.102	51.4	0.003	1.286	0.00012	0.00115	57.7	6.04	5.24
0.114	57.0	0.003	1.425	0.00012	0.00115	70.9	7.42	5.24
0.117	58.4	0.003	1.461	0.00012	0.00115	74.4	7.80	5.24
0.121	60.5	0.003	1.512	0.00012	0.00115	79.8	8.36	5.24
0.125	62.6	0.003	1.564	0.00012	0.00115	85.4	8.95	5.24
0.129	64.6	0.003	1.615	0.00012	0.00115	91.0	9.53	5.24
0.131	65.4	0.003	1.634	0.00012	0.00115	93.2	9.77	5.24
0.134	66.8	0.003	1.668	0.00012	0.00115	97.2	10.2	5.24
0.138	68.8	0.003	1.718	0.00012	0.00115	103	10.8	5.24
0.142	70.9	0.004	1.769	0.00012	0.00115	109	11.5	5.24
0.146	73.0	0.004	1.821	0.00012	0.00115	116	12.1	5.24
0.153	76.7	0.004	1.912	0.00012	0.00115	128	13.4	5.24
0.151	75.3	0.004	1.877	0.00012	0.00115	123	12.9	5.24

The units for Δv and V are in V, Δi and I are in A, and Δq" and q" are in kW/m^2. After solving for Δq", it was found that the heat flux had an overall uncertainty of 5.24%. The overall uncertainty is large enough to impact the data set; for example, at a heat flux of 128 kW/m^2, there is a chance the actual heat flux is anywhere from 121.3 to 134.7 kW/m^2. This is quite

significant when comparing the wall superheat and heat flux to generate the boiling curve, especially as the value reaching critical heat flux.

The wall superheat uncertainty is solely based on the uncertainty of the T-type thermocouples utilized in the experimentation, since the temperature difference only evaluates one variable. Omega's thermocouple reference table states the data produced has an error of 1.0˚C or 0.75% (whichever is greater) for temperatures above 0˚C.

Chapter 4. Conclusion

4.1. Conclusion

The purpose of this study was to evaluate the physical effects TiO_2 coating would have on heat transfer in pool boiling using an Aluminum 6061 substrate that had a cylindrical geometry. The two methods used to apply the TiO_2 coating did not differ much; however, the two different samples had varying results. The sample with the TiO_2 coating without the use of the NeverWet^{TM} base coating yielded the best result in heat transfer enhancement during nucleate pool boiling based on the pool boiling curves.

The uncoupled sample was significantly more hydrophilic, showed a significant increase in active nucleation sites, and had a higher bubble departure frequency than the other samples. Using Kimmie's adaptation of the Circular Hough Transform, and adapting Naccarato's droplet detection method for use in bubble detection, the bubble radii, departure frequency, and amount of bubbles were quantifiable on MATLAB. This made it simple to process those data sets to input into the Forster and Grief model. This data increased the validity of the conclusion made based on the experimental data.

Overall, the uncoupled sample showed a CHF improvement of 8% compared to the baseline sample and coupled sample results. The highest CHF found for the uncoupled sample was 143.6 kW/m^2 whereas for the baseline samples it was 128.0 kW/m^2. Furthermore, during nucleate pool boiling, the uncoupled sample had a far higher number of nucleation points and denser bubble populations than the baseline sample did – this data can also be backed up by the 3-D bar graphs displayed in Appendix B.

4.2. Pool boiling chamber design optimization

There can be significant improvement with the design of the pool boiling chamber. Starting with the material, the use of stainless steel throughout the chamber should be sufficient, as opposed to using stainless steel with PTFE plates on the sides. The PTFE plates posed an issue because when tightened too much, it would bow and cause water to leak out of the chamber – this led to a quick fix of backing up the PTFE with steel plates. Additionally, the chamber can be significantly smaller – this way there is less wait time for the water to heat up to saturation temperature. Furthermore, a total of four thermocouples should have been used to monitor the temperature of the water (for redundancy) and should have been placed near the top right, top left, bottom right, and bottom corners of the chamber. The auxiliary heater would have been best placed in the lower middle area of the chamber.

The condensing portion of the unit was also a bit of an issue. In the current design, it was difficult to maintain an equilibrium between condensing and boiling; this was largely due to physical constraints. The space where steam was travelling up to the condenser, and condensed water was coming back down to the chamber was very constricted, which would naturally cause an imbalance. For best results, a closed system that includes an internal condenser would be optimal for conducting pool boiling testing.
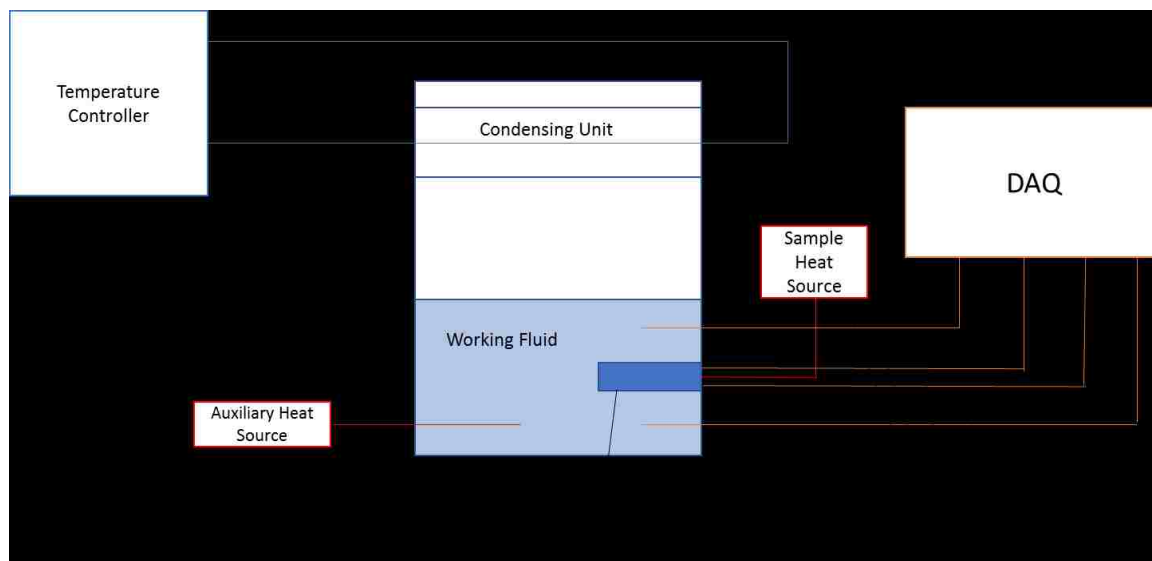
Figure 4.1: Sample drawing of suggested improvements to the experimental setup

Figure 4.1 summarizes these suggested fixes in a simple, conceptual drawing. There would be more thermocouples; however, since this is a 2D figure, thermocouples placed closer and away from the reader would be difficult to designate.

The current design also failed to account for easy water removal and sample replacement; future designs should include a drain and a method to easily replace samples. With the current design, the chamber needed to be taken apart after every test to replace the sample and to drain the water. Optimizing the design this way would save a lot of time and give the user more opportunities to test various samples.

4.3. Suggested future work

The appropriate next step to this study would be to take advantage of the photosensitive properties of TiO_2 and conduct a nucleate pool boiling study of TiO_2 coated Al 6061 after being exposed to UV light for varying amounts of time. Similar studies have been conducted with square heaters and for copper substrates, but it would be interesting to see the observations made

using an aluminum substrate and a cylindrical geometry, and if it would result in an even further

enhancement in heat transfer in pool boiling.
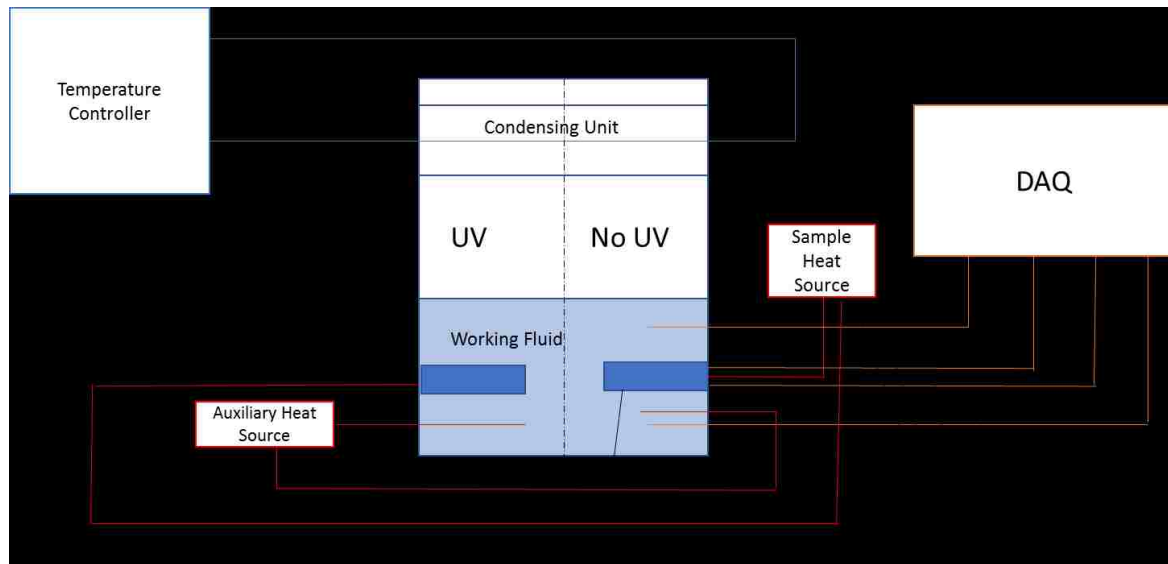
Figure 4.2: Suggested design for future study with UV treatment

Figure 4.2 takes the design of Figure 4.1 and modifies it in a way to evaluate UV irradiated

samples. A welded wall can be included in the center of the chamber (displayed as a dashed line)

so that the system can maintain proper equilibrium and have a proper division. Insulation should

also be applied at this wall in order to maintain integrity of the heat applied in each individual

system. This enables the user to simultaneously observe the effects UV irradiation has on TiO_2

during pool boiling and provide the user with a baseline at the same time.

Another study that would be appropriate to follow this one, would be to create a finite element model of the pool boiling system. Two-phase models have been done before; however, there is a challenge in modeling a sample with specific grooves, cavities, or micro/nano-structures and coupling the physics of such materials with the typical two-phase flow physics (Navier-Stokes, Energy Balance, etc.). Modeling pool boiling heat transfer on a cylindrical or flat surface with TiO_2 coating and an aluminum substrate would be great to compare with the experimental data found in this thesis and other papers and other models such as Forster and Greif's vapor-exchange model.

Appendix A: Plots of trials of pool boiling data for each sample.

      Appendix A provides the pool boiling curve plots generated by individual trials for each

type of test conducted.

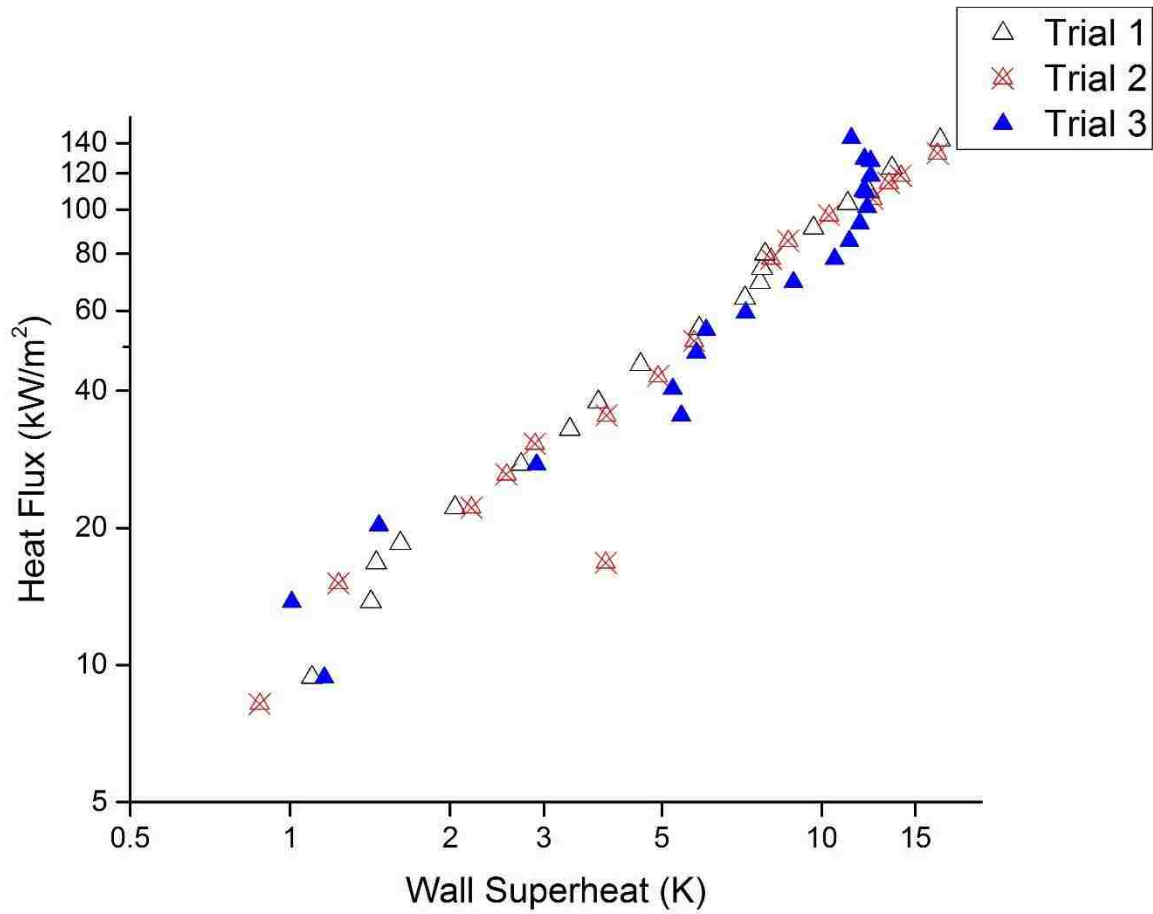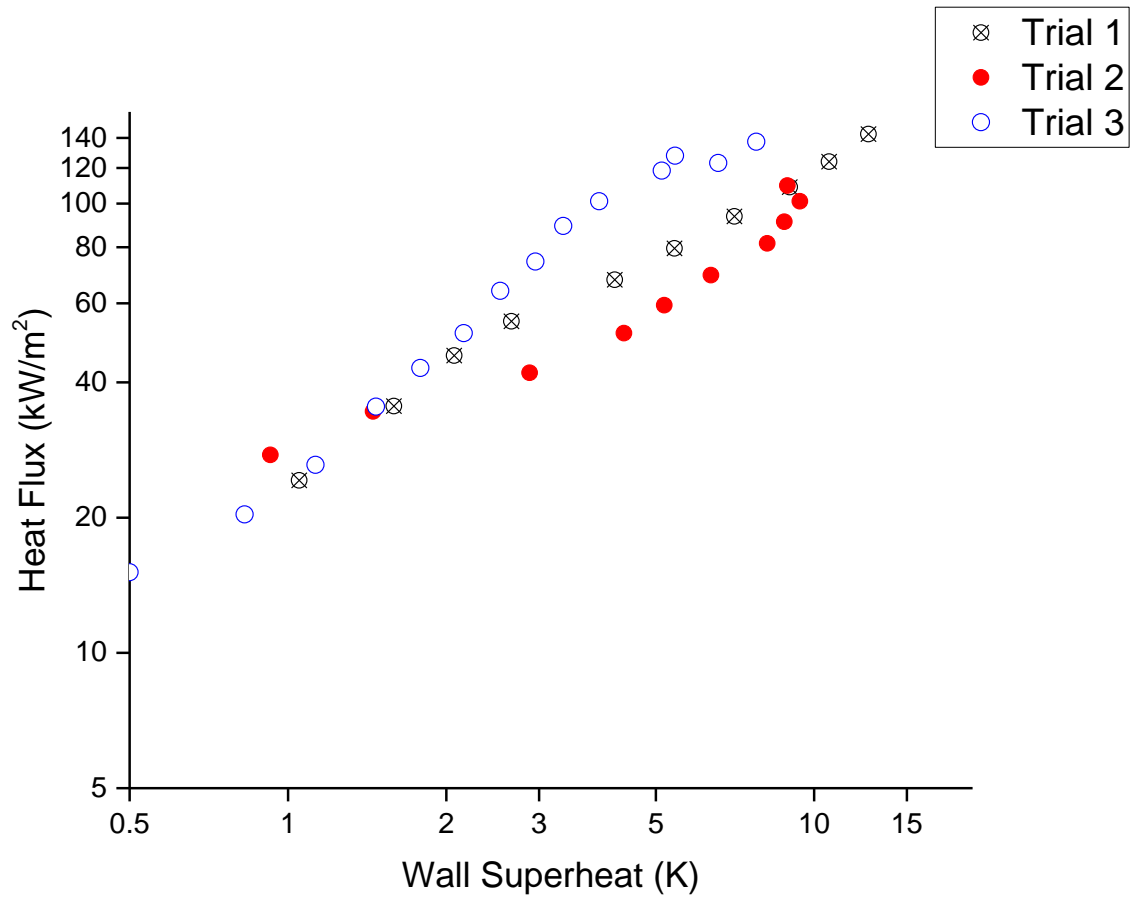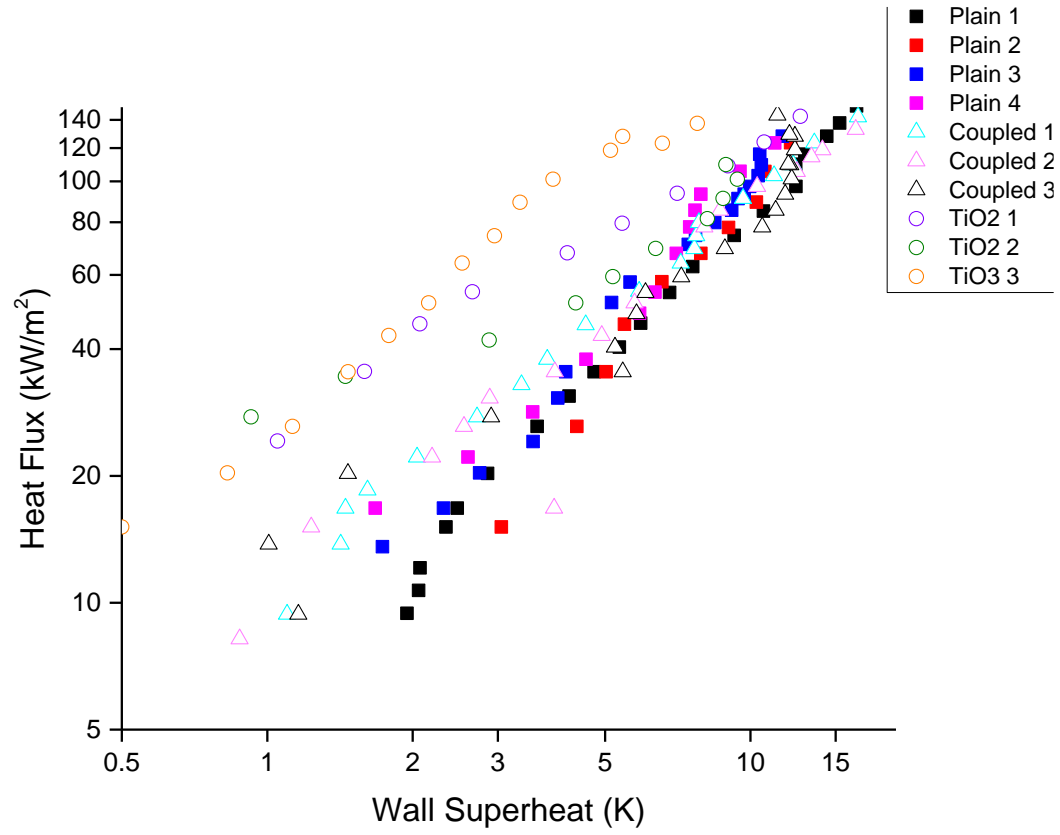Pool boiling curve of TiO_2 coated Al 6061 with NeverWet[TM] base coating:

Figure 4.3: Pool boiling curve of the trials attempted with TiO_2 coated with NeverWet[TM]

Pool Boiling Curve of TiO₂ without the NeverWet^{TM} base coating:

Figure 4.4: Pool boiling curve of TiO2 coated Al 6061 with no coupling agent.

All Trials:

**Figure 4.5: Boiling curve individualized by trial**

Appendix B: CHT histograms at varying frames and heat fluxes.

      The data produced by the modified CHT was used to gather data such as bubble count an diameter per frame. In this appendix, samples of the total collected data can be found on 3-D plots for the tested samples at three varying heat fluxes. This is to give the reader an idea of the difference of the results produced by a baseline sampled, and a coated substrate.

Plain Aluminum 6061

$q" = 40$ kW/m^2:
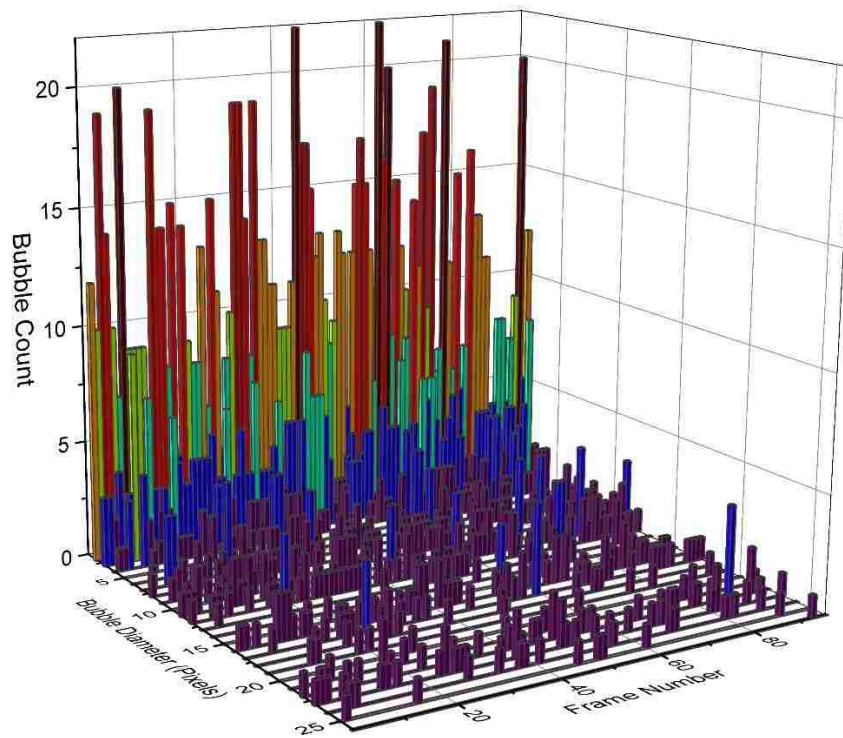
Figure 4.6: Bubble count at each diameter per frame (40 kW/m^2)

q" = 67 kW/m^2
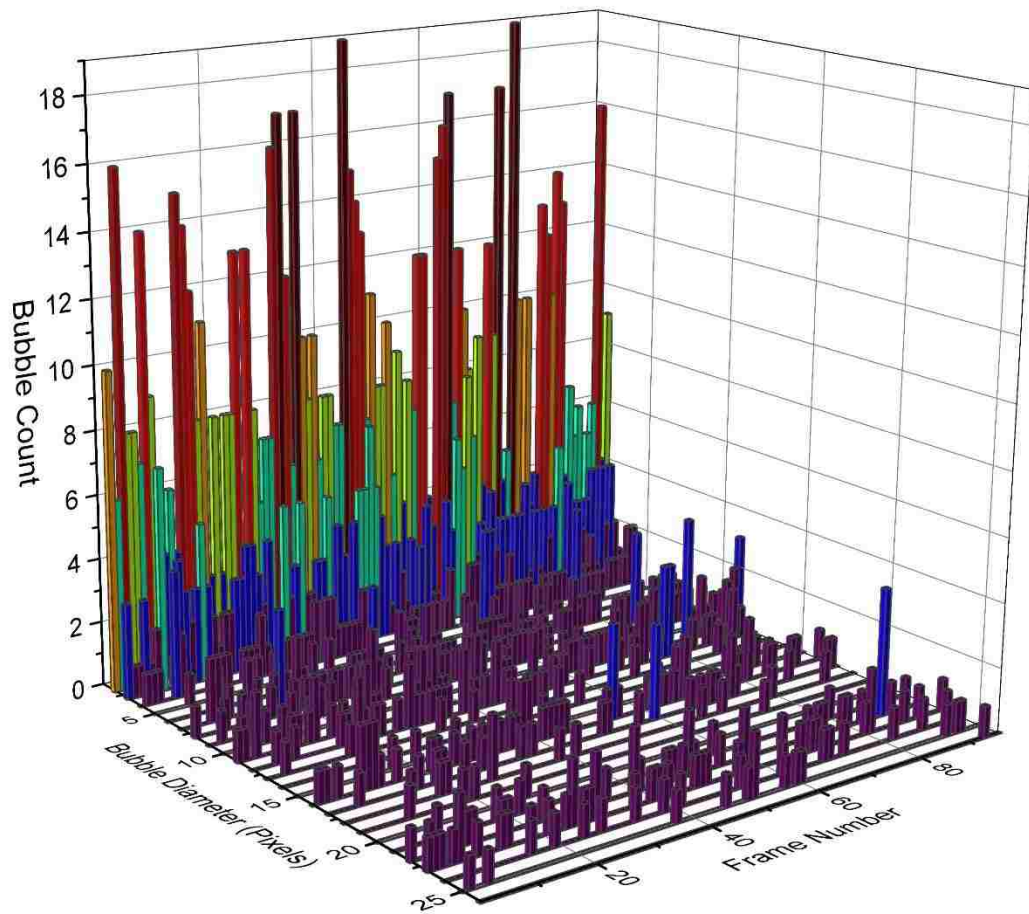
Figure 4.7: Bubble count at each diameter per frame (67 kW/m^2)

q" = 120 kW/m

Figure 4.8: Bubble count at each diameter per frame (120 kW/m^2)

The highest bubble count recorded with the baseline samples did not surpass 40 for any frame at each heat flux captured. The difference can be seen with the TiO$_2$ coated data (without coupling).

TiO$_2$ Coated Aluminum 6061

q" = 40 kW/m^2:
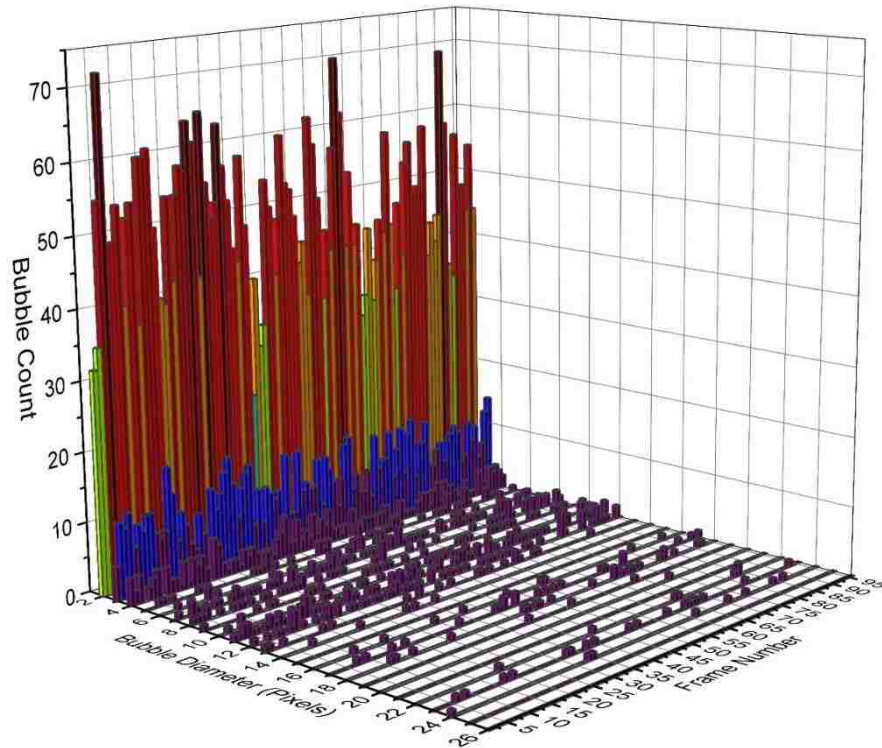
Figure 4.9: Bubble count at each diameter per frame (40 kW/m^2)
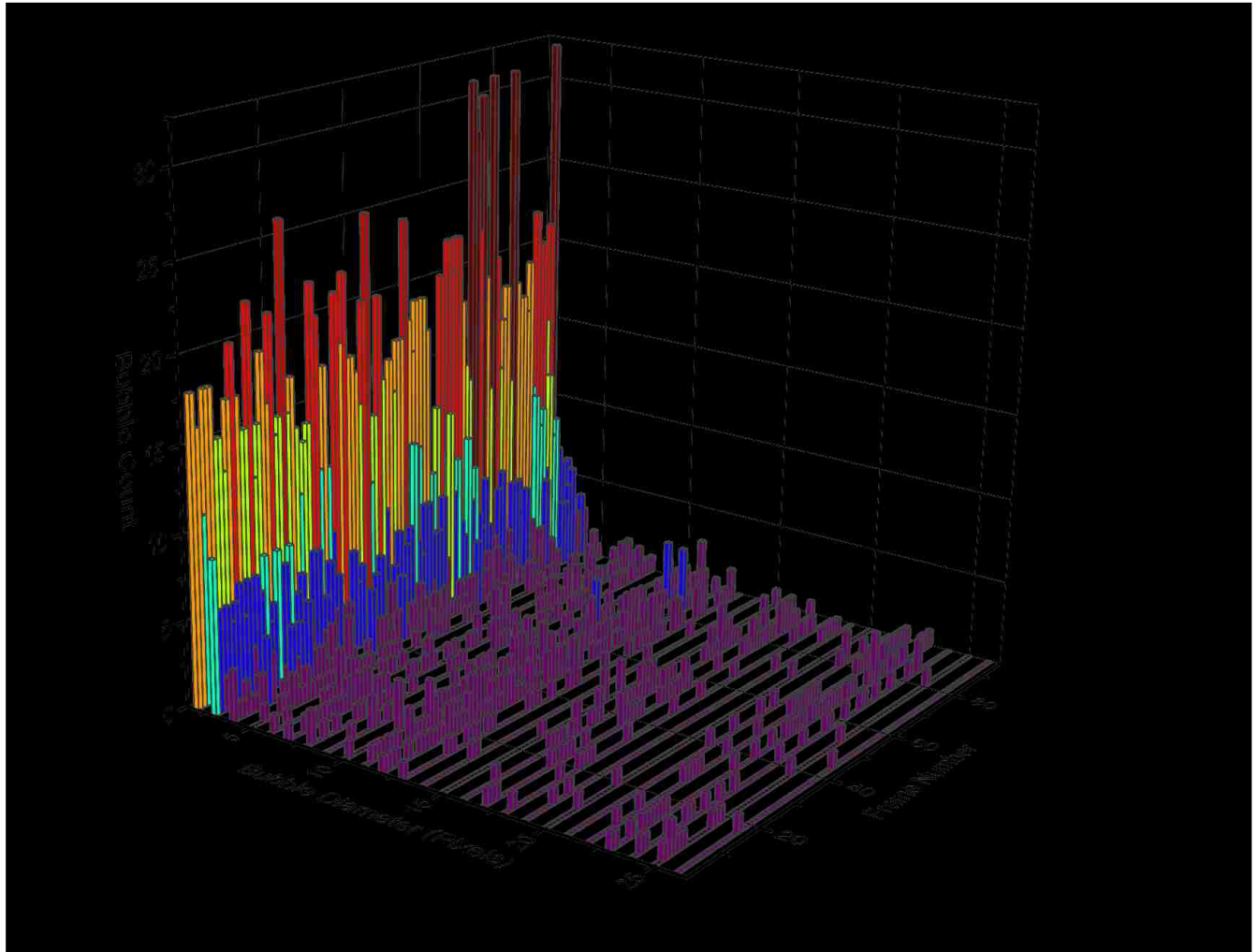
Figure 4.10: Bubble count at each diameter per frame (60 kW/m^2)

q" = 120 kW/m^2
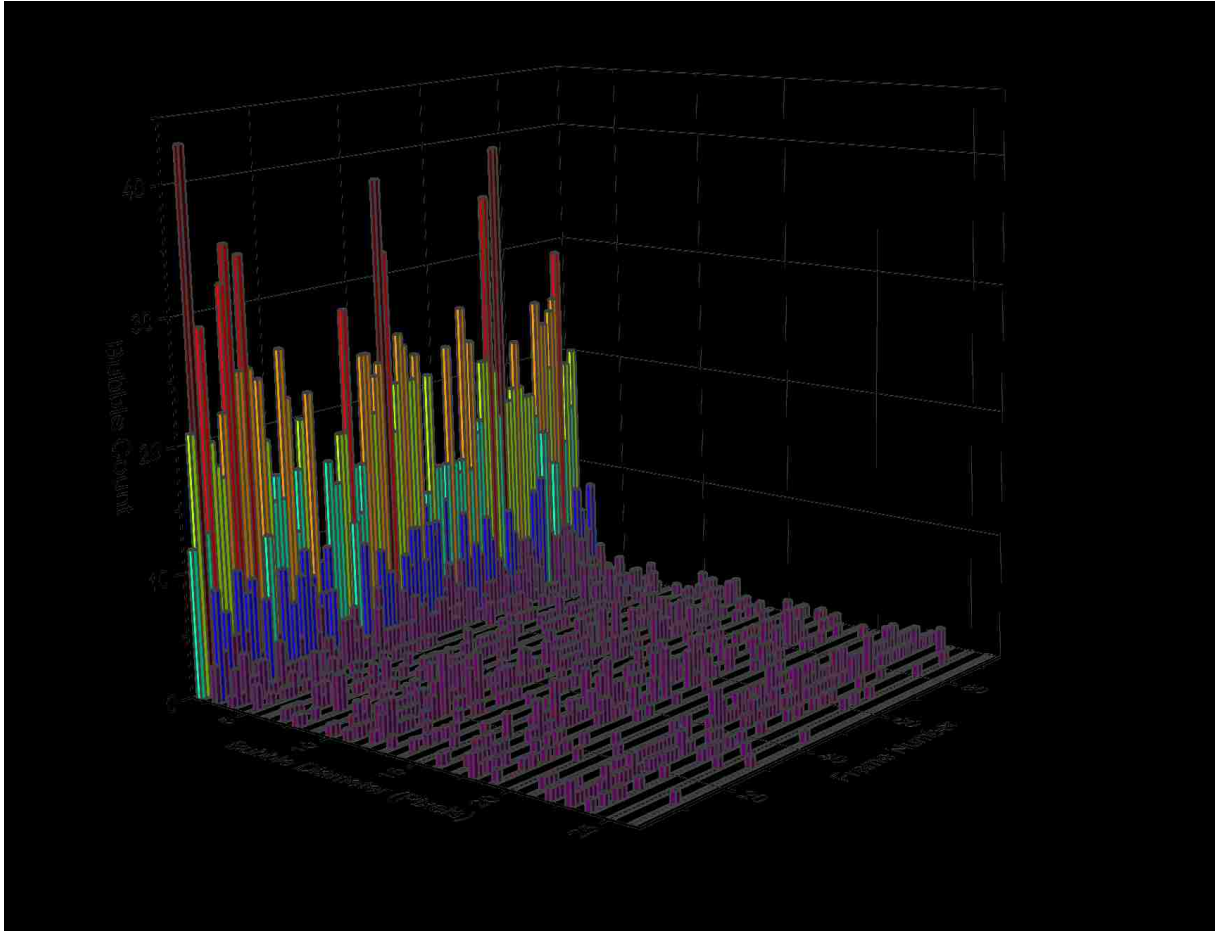
Figure 4.11: Bubble count at each diameter per frame (120 kW/m^2)

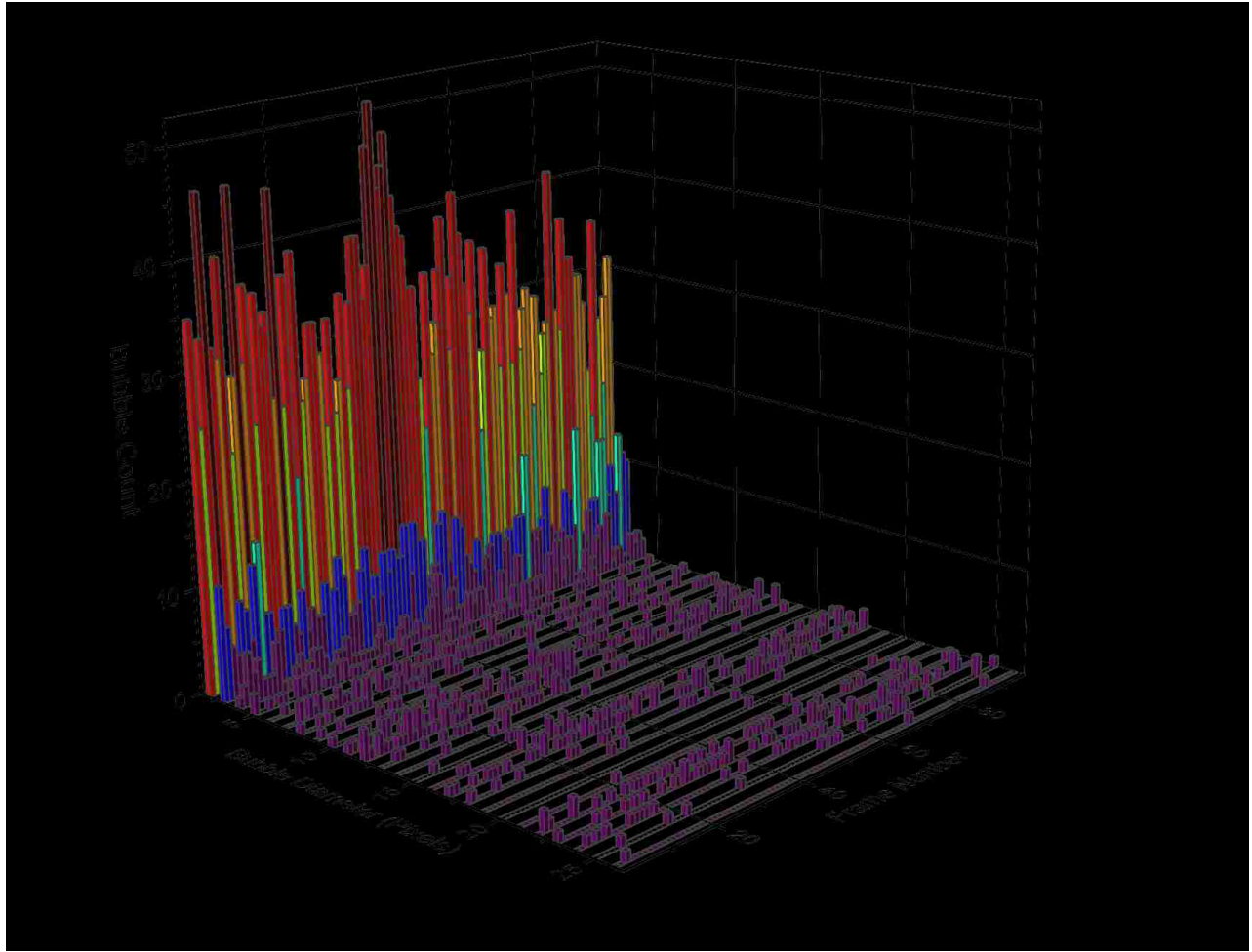As the heat flux gets higher, the overall bubble count goes down; however, the count of bubbles with larger diameter increases.

Appendix C: Boiling curve video footage

Pool boiling videos will be uploaded to ProQuest as supplemental videos.

Bibliography

[1]   Incropera, F. P., DeWitt, D. P., Bergman, T. L., and Lavine, A. S., 2007, *Fundamentals of Heat and Mass Transfer*, John Wiley & Sons.

[2]   Forster, H. K., and Greif, R., 1959, "Heat Transfer to a Boiling Liquid Mechanism and Correlations," J. Heat Transf., **81**, pp. 43–54.

[3]   Sabersky, R. H., and Mulligan, H. E., 1955, "On the Relationship Between Fluid Friction and Heat Transfer in Nucleate Boiling," Jounral Jet Propuls., **25**(1), pp. 9–12.

[4]   Tsien, H. (California I. of T., 1952, "Private Communications."

[5]   Dhillon, N. S., Buongiorno, J., and Varanasi, K. K., 2015, "Critical Heat Flux Maxima during Boiling Crisis on Textured Surfaces," Nat. Commun., **6**, p. 8247.

[6]   Young Lee, C., Hossain Bhuiya, M. M., and Kim, K. J., 2010, "Pool Boiling Heat Transfer with Nano-Porous Surface," Int. J. Heat Mass Transf., **53**(19–20), pp. 4274–4279.

[7]   Wu, W., Bostanci, H., Chow, L. C., Hong, Y., Su, M., and Kizito, J. P., 2010, "Nucleate Boiling Heat Transfer Enhancement for Water and FC-72 on Titanium Oxide and Silicon Oxide Surfaces," Int. J. Heat Mass Transf.

[8]   Zhang, B. J., 2012, "Nucleate Pool Boiling of Surface-Modified Nano-Porous Alumina."

[9]   Zhang, B. J., Hwang, T., Nam, J.-D., Suhr, J., and Kim, K. J., 2014, "Noncovalently Assembled Nanotubular Porous Layers for Delaying of Heating Surface Failure," Sci. Rep., **4**, p. 6817.

[10]   Zhang, B. J., Kim, K. J., and Yoon, H., 2012, "Enhanced Heat Transfer Performance of Alumina Sponge-like Nano-Porous Structures through Surface Wettability Control in Nucleate Pool Boiling," Int. J. Heat Mass Transf., **55**(25–26), pp. 7487–7498.

[11]   Takata, Y., Hidaka, S., Cao, J. M., Tanaka, K., Masuda, M., Ito, T., Watanabe, T., and Shimohigoshi, M., 2000, "Boiling and Evaporation from a Superhydrophilic Surface," Therm. Sci. Eng., **8**(6), pp. 33–41.

[12]   Wang, R., and Hashimoto, K., 1997, "Light-Induced Amphiphilic Surfaces," Nature, **388**, pp. 431, 432.

[13]   Inc., A. S. M., "Aluminum 6061-T6; 6061-T651" [Online]. Available: http://asm.matweb.com/search/SpecificMaterial.asp?bassnum=ma6061t6.

[14]   Kline, S. J.; McClintock, F. A., 1953, "Describing the Uncertainties in Single Sample Experiments," Mech. Eng., pp. 3–8.

[15]   2017, "Keysight N5700 Series Data Sheet."

[16]   (Omega), "Omega Revised Thermocouple Reference Table - Type T."

[17]   Mo, S. Di, and Ching, W. Y., 1995, "Electronic and Optical Properties of Three Phases of Titanium Dioxide: Rutile, Anatase, and Brookite," Phys. Rev. B, **51**(19), pp. 13023–13032.

[18]   Cromer, D. T., and Herrington, K., 1955, "The Structures of Anatase and Rutile," J. Am. Chem. Soc., **77**(18), pp. 4708–4709.

[19]   Srivastava, A. K., Deepa, M., Bhandari, S., and Fuess, H., 2009, "Tunable Nanostructures and Crystal Structures in Titanium Oxide Films," Nanoscale Res. Lett., **4**(1), pp. 54–62.

[20]   "NeverWet Technical Data Sheet."

[21]   Cheng, B. K., Naccarato, B., Kim, K. J., and Kumar, A., 2016, "Theoretical Consideration of Contact Angle Hysteresis Using Surface-Energy-Minimization Methods," Int. J. Heat Mass Transf., **102**, pp. 154–161.

[22]   Lin, J., Banerji, S., and Yasuda, H., 1994, "Role of Interfacial Tensions in the Formation

and the Detachment of Air Bubbles. 2. A Single Orifice on an Inclined Plane Immersed in Water," Langmuir, (12), pp. 943–948.

[23]   Hsu, Y. Y., 1962, "On the Size Range of Active Nucleation Cavities on a Heating Surface," J. Heat Transfer, **84**(3), pp. 207–213.

[24]   Bhuiya, H., 2008, "University of Nevada , Reno A Feasibility Study : Nano Tailored Surfaces for Enhanced Heat Transfer A Thesis Submitted in Partial Fulfillment of the Requirements for the Degree of Master of Science in Mechanical Engineering by Md Mainul Hossain Bhuiya Dr."

[25]   Kimme, C., Ballard, D., and Sklansky, J., 1975, "Finding Circles by an Array of Accumulators," Commun. ACM, **18**(2), pp. 120–122.

[26]   Duda, R. O., and Hart, P. E., 1972, "Use of the {H}ough Transform to Detect Lines and Cures in Pictures," Commun. Assoc. Comput. Mach., **15**(1), pp. 11–15.

[27]   Naccarato, B., 2017, "Visualization of Dropwise Condensation on Vertical Plate and Horizontal Tube Geometry," (August).

[28]   Thompson, C.; Shure, L., 1993, "Image Processing Toolbox: For Use with MATLAB."

[29]   Sobel, I., and Feldman, G., 1973, "A 3x3 Isotropic Gradient Operator for Image Processing.," Hart, P. E. Duda R. O. Pattern Classif. Scene Anal., pp. 271–272.

Curriculum Vitae

Kevin Yim
kevin.yim@unlv.edu

EDUCATION

University of Nevada Las Vegas, *Las Vegas, NV*, Master of Science in Mechanical Engineering, **GPA: 3.78**
August 2018 *Organizations:* Tau Beta Pi

University of Nevada Las Vegas, *Las Vegas, NV*, Bachelor of Science in Mechanical Engineering, **GPA: 3.03**
May 2014
Honors and Awards: Governor Guinn Millennium Scholarship, Army ROTC Scholarship, Dean's Honor List
(Spring 2014)

SPECIALIZED SKILLS/STRENGTHS

Software: MATLAB, SolidWorks, Autodesk Fusion, COMSOL, LabVIEW, Microsoft Office (PowerPoint, Excel,
Word)
Instruments: Optical Microscope, Contact Angle Goniometer, Scanning Electron Microscope
Certifications: EIT/FE (Nevada), OSHA 30-hour, Active DoD Security Clearance

ENGINEERING EXPERIENCE

Mechanical Engineer II – Thermal Analyst, *Raytheon Missile System*, Tucson, AZ   **Start Date Pending**

Graduate Research Assistant, *University of Nevada Las Vegas,* Las Vegas, NV   **Summer 2016, May 2017 -
Present**
- Researched changes in heat transfer in pool boiling by varying surface geometry, surface treatments, and
  material.
- Designed and built a pool boiling chamber and tested aluminum with varying surface geometry and
  compared the resulting experimental boiling curve data sets with a finite element model using COMSOL.
- Used MATLAB to conduct video analysis with footage from a high-speed camera to obtain visualization
  data from the pool boiling experiments.
- Gathered 3D surface profiles of the tested samples using an optical microscope to produce multi-physics
  models on COMSOL and collected material structure information using a scanning electron microscope to
  investigate the observed changes in heat transfer in pool boiling.

Graduate Teaching Assistant, *University of Nevada Las Vegas*, Las Vegas, NV   **Aug 2015 – May 2017**
- Taught PID Controls Laboratory during Fall semesters to classes of 20. Instructed students on the effects of
  varying parameters of PID controllers using MATLAB/Simulink and controls applications to dynamic and
  thermo-fluid systems.
- Instructed Engineering Instrumentations Laboratory during Spring semesters to classes of 20. Acquainted
  students with the fundamentals of LabVIEW, DMM, ADC conversions, Fast Fourier Transforms, and
  various filters.

PIRE Research Assistant, *Korea Advanced Institute of Science and Technology,* Daejeon, South Korea   **Jul 2016**
- Collaborated with international students and investigated super-hydrophobic enhancement using elastomers
  such as PDMS and various surface treatment ideas using bio-mimicry to enhance heat transfer in nucleate
  pool boiling.
- Submitted a poster of PDMS research and soft robotics research conducted to the American Society of
  Engineering Education Conference (April 2017).

Mechanical Engineering Intern, *Unilever,* Henderson, NV   **May 2015 – Aug 2015**
- Served as a Project Lead and worked with 7 engineering and maintenance technicians to ensure the HVAC
  systems and Waste Water Pre-Treatment Plant (WWTP) were complying with the Process Safety
  Management Program.

- Developed and published Standard Operating Procedures (SOPs) on equipment and daily activity of the WWTP.
- Reduced costs for the engineering services department by thousands of dollars per month by replacing waste water treatment chemicals with a more cost-effective version after conducting tests with various flocculants.

MILITARY LEADERSHIP EXPERIENCE

Squadron Communications Officer, *NV Army National Guard,* Las Vegas, NV   **May 2016 - Present**
- 1 of 8 primary staff officers; responsible for all C4 equipment for an organization of over 600 Soldiers.
- Led a multi-million-dollar initiative to transform a vacant area into a Secret-level TOC and submitted plans, drawings, and required material to the state staff.
- Completed 3 training events (1 in Korea) with 0 loss of command and control within the Squadron.
- Evaluated as the top staff officer in the organization and rated in the top 10% of lieutenants (out of 19).

Expeditionary Signal Platoon Leader, *NV Army National Guard,* Las Vegas, NV   **May 2014 – May 2016**
- Led a platoon consisting of 46 personnel and $8 million in equipment including 6 nodes of communication.
- Planned and executed 3 exercises that resulted in the platoon validating 100% of communication nodes and establishing voice/data networks with the capability of supporting 400 users.
- Developed younger, less experienced Soldiers by enabling them with lead roles during validation missions.
- Rated as "Excels" (top rating) by the company commander.